Extension of the Bayesian searches for anisotropic stochastic gravitational-wave background with nontensorial polarizations

Leo Tsukada[*]

Department of Physics, The Pennsylvania State University, University Park, Pennsylvania 16802, USA and Institute for Gravitation and the Cosmos, The Pennsylvania State University, University Park, Pennsylvania 16802, USA

(Received 20 August 2023; accepted 6 November 2023; published 15 December 2023)

The recent announcement of strong evidence for a stochastic gravitational-wave background (SGWB) by various pulsar timing array collaborations has highlighted this signal as a promising candidate for future observations. Despite its nondetection by ground-based detectors such as Advanced LIGO and Advanced Virgo, Callister *et al.* [Phys. Rev. X **7**, 041058 (2017)] developed a Bayesian formalism to search for an isotropic SGWB with nontensorial polarizations, imposing constraints on signal amplitude in those components that violate general relativity using LIGO's data. Since our ultimate aim is to estimate the spatial distribution of gravitational-wave sources, we have extended this existing method to allow for anisotropic components in signal models. We then examined the potential benefits from including these additional components. Using injection campaigns, we found that introducing anisotropic components into a signal model led to more significant identification of the signal itself and violations of general relativity. Moreover, the results of our Bayesian parameter estimation suggested that anisotropic components aid in breaking down degeneracies between different polarization components, allowing us to infer model parameters more precisely than through an isotropic analysis. In contrast, constraints on signal amplitude remained comparable in the absence of such a signal. Although these results might depend on the assumed source distribution on the sky, such as the Galactic plane, the formalism presented in this work has laid a foundation for establishing a generalized Bayesian analysis for an SGWB, including its anisotropies and nontensorial polarizations.

DOI: 10.1103/PhysRevD.108.124042

I. INTRODUCTION

In recent years, there has been a dramatic expansion in the field of gravitational wave (GW) astronomy, driven by the consistent detection of such signals by the LIGO Scientific, Virgo and KAGRA Collaboration (LVK) [1–4]. The GWs observed to date have come from compact binary coalescence (CBC) such as binary black hole (BBH) [5–12] and binary neutron star (BNS) [13,14]. Detailed studies of these astrophysical events have enhanced our understanding of general relativity, nuclear physics, and the astrophysical processes involved in such mergers, thus providing a unique perspective into the Universe. Moreover, the recent announcement regarding strong evidence for an stochastic gravitational-wave background (SGWB) by several pulsar timing array (PTA) collaborations [15–18] has propelled this field forward with the potential detection of an SGWB, introducing a potential new avenue in the nHz frequency band to observe GWs.

An SGWB is the incoherent superposition of GWs emitted from numerous sources, which are too faint to be individually resolved (see e.g., [19] for a detailed review). It is primarily composed of astrophysical sources such as super-massive black hole (SMBH) binaries [20–25], targeted by the PTA collaborations, along with stellar BBHs or BNSs [26–30], and supernovae [31–35]. Alternatively, cosmological sources, including signals emitted during the inflationary era [36–44], phase transitions in the early Universe [45–47], and primordial primordial black holes (BHs) [48–51], can contribute to the SGWB. Despite the promising results from the PTA collaborations, ground-based detectors like Laser Interferometer Gravitational-wave Observatory (LIGO) [52] and Virgo [53] have not made any substantial detections. This is largely because they are tuned to higher frequency GWs produced by events within a relatively nearby Universe, whereas a considerable portion of the SGWB signal falls into the low-frequency regime. Since May 2023, with further improved sensitivities of LIGO and Virgo, the expanded detector network including KAGRA [54] has begun the fourth observing run, aiming for the novel discovery of a SGWB signal.

As one of the physical implications from GW observations, there have been extensive studies that examine the theories of gravity by investigating the violation of general

[*]leo.tsukada@ligo.org

relativity in GW observations [55–59]. These include (but are not limited to) the parametrized tests of the post-Newtonian coefficients [60–64], the speed of GWs [65], black-hole nature of the merger remnant [66–72] and, most relevant to this work, the nontensorial GW polarizations [12,56,73–78]. Regarding the GW polarization analyses, Ref. [73] demonstrates the method to search for a GW signal from a CBC, which is purely polarized with either one of three polarizations, i.e. *scalar* or *vector* or *tensor*. This method was adopted for the analysis of GW170814 [9] and GW170817 [56], which were consequently reanalyzed with modified waveforms [74] and tensor-scalar mixed polarization model [75], respectively. Alternatively, Ref. [76] demonstrates the use of *null streams*, constructed by a GW model with the tensor polarizations, as a model-independent way to assess the GW polarization contents violating the prediction from general relativity. They find that the independent measurement of each GW polarization for transient GW signals requires the same number of detectors as the polarization modes to measure, which leaves up to five detectors.[1] References [77,78] apply this approach to GW170817 and obtain a constraint of GW amplitude for the vector polarization or p-values for the nontensorial polarization hypothesis.

As opposed to the limitation for polarization measurements in such a transient GW signal, unpolarized SGWBs[2] allow for measuring or constraining the background amplitude for each of the three GW polarizations separately. In the context of ground-based GW detectors, Ref. [80] first explores the detectability of an SGWB with nontensorial polarizations based on a frequentist approach by deriving signal-to-noise ratio (SNR) for arbitrary polarization contents, finding that the separate measurement of generic GW polarization contents require at least three detectors. Alternatively, Ref. [81] demonstrates a *Bayesian* framework to search for each polarization component of an isotropic SGWB with a broadband frequency spectrum. More specifically, it provides a statistical prescription to assess the presence of nontensorial polarizations based on a Bayes factor as well as posterior results of given model parameters as a way of parameter estimation. Following this method, Refs. [82–84] search for nontensorial polarization components of an SGWB in LVK's dataset up to the third observing run.

In this work, we extend the Bayesian framework introduced by Ref. [81] to account for *anisotropies* of an SGWB. Several searches for anisotropic SGWBs contributed from either pointlike or extended sources have been developed and performed for LVK's dataset. While pixel-wise radiometer methods [85–87] are intended for pointlike sources, one of the common approaches for extended sources is the use of the spherical harmonics (SPH) expansion of an anisotropic SGWB signal in cross spectral density (CSD) $C(f,t)$, which reads [88,89]

$$\langle C(f,t)\rangle = \sum_{\mu\in\{(\ell,m)\}} \gamma_\mu(f,t)\mathcal{P}_\mu(f). \tag{1}$$

Here, $\gamma_\mu(f,t)$ is referred to as the overlap reduction function (ORF) [90] projected onto the SPH basis represented by $\mu=(\ell,m)$ [91], and $\mathcal{P}_\mu(f)$ is a generic form of a spectral model with the anisotropic distribution. The Greek subscript implies the summation across the SPH modes. Reference [89] incorporates this expression into the Bayesian framework of an isotropic SGWB to include its anisotropies and provide detection statistics as well as posterior results for an assumed source distribution on the sky. Reference [92] explores the possibility to reconstruct a SGWB intensity map using marginalized posterior distributions. In this paper, we essentially combine the formalisms developed by Refs. [81,89] and establish a generalized Bayesian analysis for an SGWB including anisotropies *and* nontensorial polarizations.

This paper is structured as follows. Section II presents the role and derivation of ORF in the context of ground-based GW detectors. In particular, we compute the ORF projected onto the SPH basis for the nontensorial polarizations as a key ingredient for this analysis. In Sec. III, focusing on the Bayesian formalism as a versatile tool for the data analysis in this work, we provide an overview of the Bayesian framework and applications to the detection and parameter estimation of an anisotopic SGWB. Proceeding to Sec. IV, we demonstrate how to identify an anisotropic SGWB signal with the nontensorial polarizations using a simulated noise dataset for the two LIGO detectors. Specifically, a synthetic anisotropic SGWB signal is injected into the dataset and recovered with either isotropic or anisotropic SGWB model and we compare the detection capability between the two cases. Finally, in Sec. V, we investigate the results of parameter estimation to quantify the measurement accuracy for the model parameters of an injected SGWB signal such as amplitude and frequency spectrum, demonstrating various benefits gained by incorporating higher SPH modes into a signal model.

II. OVERLAP REDUCTION FUNCTION

A. Formalism

As mentioned in Eq. (1), an SGWB signal is imprinted in the CSD estimator, multiplied with a scaling factor and phase shift, which are determined by a baseline's geometry and relative orientation and represented by the ORF $\gamma(f)$. Hence, this encodes the sensitivity of a given baseline to an SGWB as a function of frequencies. In the context of

[1]Note that the scalar longitudinal and breathing modes indicate complete degeneracy in their antenna responses [see Eq. (14)] of the current ground-based detectors.

[2]Ref. [79] pointed out that one cannot necessarily apply the model-independent formalism as some of the assumptions break down in beyond-GR theories, e.g. Chern-Simons gravity. Nevertheless, this is beyond the scope of this paper and we leave this as a potential avenue to pursue in the future.

searches for anisotropic SGWBs, in general the ORF also depends on time due to the Earth's rotation with respect to the cosmological rest frame. Specifically, at a particular point on the sky $\hat{\mathbf{\Omega}}$, this is given by[3] [90,93–95]

$$\gamma^I(f,t,\hat{\mathbf{\Omega}}) = \frac{5}{8\pi}\sum_A F_1^A(\hat{\mathbf{\Omega}},t)F_2^A(\hat{\mathbf{\Omega}},t)\mathrm{e}^{2\pi i f\frac{\hat{\mathbf{\Omega}}\cdot\mathbf{\Delta}x_I(t)}{c}}, \quad (2)$$

where $\mathbf{\Delta}x_I(t)$ is the time-dependent separation vector between the two detectors in a baseline I.

$F_i^A(\hat{\mathbf{\Omega}},t)$ is the ith detector's antenna pattern response function for the polarization A, which reads

$$F_i^A(\hat{\mathbf{\Omega}},t) = d_i^{\mu\nu}(t)e_{\mu\nu}^A(\hat{\mathbf{\Omega}}). \quad (3)$$

$d_i^{\mu\nu}(t)$ is the response tensor of ith detector as follows

$$\boldsymbol{d}_i(t) = \frac{1}{2}(\hat{\boldsymbol{X}}(t)\otimes\hat{\boldsymbol{X}}(t) - \hat{\boldsymbol{Y}}(t)\otimes\hat{\boldsymbol{Y}}(t)), \quad (4)$$

where $\hat{\boldsymbol{X}}(t), \hat{\boldsymbol{Y}}(t)$ are the time-dependent unit vectors that define the direction of detector's x or y-arm respectively, and $\otimes$ represents a tensor product. $e_{\mu\nu}^A(\hat{\mathbf{\Omega}})$ is the polarization tensor, defined commonly on the *GW frame*, in which $\hat{\mathbf{\Omega}}$ is equivalent to the unit vector pointing at a GW source, and $\hat{\boldsymbol{m}}$, $\hat{\boldsymbol{n}}$ are a pair of orthogonal unit vectors in the plane perpendicular to $\hat{\mathbf{\Omega}}$. Using these bases, for the two modes $A = \{+,\times\}$ expected from general relativity, the polarization tensors are expressed as

$$\boldsymbol{e}^+(\hat{\mathbf{\Omega}}) = \hat{\boldsymbol{m}}\otimes\hat{\boldsymbol{m}} - \hat{\boldsymbol{n}}\otimes\hat{\boldsymbol{n}} \quad (5)$$

$$\boldsymbol{e}^\times(\hat{\mathbf{\Omega}}) = \hat{\boldsymbol{m}}\otimes\hat{\boldsymbol{n}} + \hat{\boldsymbol{n}}\otimes\hat{\boldsymbol{m}}. \quad (6)$$

As a reference, once putting these together, using Euler angles (θ,ϕ,ψ) in the *detector frame*, whose x and y axes point toward detector's arms, the antenna pattern response functions for the two modes read

$$F^+(\theta,\phi,\psi) = \frac{1}{2}(1+\cos^2\theta)\cos 2\phi\cos 2\psi - \cos\theta\sin 2\phi\sin 2\psi, \quad (7)$$

$$F^\times(\theta,\phi,\psi) = -\frac{1}{2}(1+\cos^2\theta)\cos 2\phi\cos 2\psi - \cos\theta\sin 2\phi\cos 2\psi. \quad (8)$$

[3]Note that the expression in Eq. (2) is normalized such that in the case of a colocated and coaligned detector pair $\int \mathrm{d}\hat{\mathbf{\Omega}}\gamma(f,t,\hat{\mathbf{\Omega}}) = 1$ at any frequency for the *tensor* polarization, and hence the those for vector or scalar polarizations represent values relative to the tensor counterpart.

To adapt to an SGWB search for extended sources, the ORF is projected from the pixel basis to the SPH basis

$$\gamma^I_{\ell m}(f,t) = \int_{S^2}\mathrm{d}\hat{\mathbf{\Omega}}\gamma^I(f,t,\hat{\mathbf{\Omega}})Y^*_{\ell m}(\hat{\mathbf{\Omega}}), \quad (9)$$

where $Y_{\ell m}$ is the (ℓ,m) mode of the SPH function defined on the cartesian coordinate whose z-axis points to the Earth's rotation axis. This SPH-based ORF has been analytically and numerically derived for the tensor polarizations in the literature [91,95]. This illustrates sensitivity to an SGWB with the spatial scale characterized by (ℓ,m) at each frequency bin for a given baseline's geometry and orientation. For example, as described in Appendix A, the ORF for $\ell = 1$ or 2 the global peak lies at frequencies below 100 Hz, while for $\ell \geq 5$ the peak appears at higher frequencies. This can be understood by the diffraction limit which each baseline is associated with due to the separation between the two detectors, i.e. the spatial resolution of signal components with lower frequencies tends to be limited by some angular resolution. In what follows, we explore the extension of the SPH-based ORF to nontensorial GW polarizations, i.e. scalar and vector polarizations.

B. Extension to the nontensorial polarizations

The ORF's dependence on the GW polarization boils down to the polarization tensor, $e_{\mu\nu}^A(\hat{\mathbf{\Omega}})$. For the nontensorial polarization modes, these tensors read[4]

$$\boldsymbol{e}^b(\hat{\mathbf{\Omega}}) = \hat{\boldsymbol{m}}\otimes\hat{\boldsymbol{m}} + \hat{\boldsymbol{n}}\otimes\hat{\boldsymbol{n}} \quad (10)$$

$$\boldsymbol{e}^\ell(\hat{\mathbf{\Omega}}) = \hat{\mathbf{\Omega}}\otimes\hat{\mathbf{\Omega}} \quad (11)$$

$$\boldsymbol{e}^x(\hat{\mathbf{\Omega}}) = \hat{\boldsymbol{m}}\otimes\hat{\mathbf{\Omega}} + \hat{\mathbf{\Omega}}\otimes\hat{\boldsymbol{m}} \quad (12)$$

$$\boldsymbol{e}^y(\hat{\mathbf{\Omega}}) = \hat{\boldsymbol{n}}\otimes\hat{\mathbf{\Omega}} + \hat{\mathbf{\Omega}}\otimes\hat{\boldsymbol{n}}, \quad (13)$$

where the superscripts denote breathing (b), longitudinal (ℓ), vector-x (x) and vector-y (y) modes, respectively. These polarization tensors lead to the antenna pattern response function for each polarization as follows

$$F^b(\theta,\phi,\psi) = -F^\ell(\theta,\phi,\psi) = \frac{1}{2}\sin^2\theta\cos 2\phi, \quad (14)$$

$$F^x(\theta,\phi,\psi) = \sin\theta(\cos\theta\cos 2\phi\cos\psi - \sin 2\phi\sin\psi), \quad (15)$$

$$F^y(\theta,\phi,\psi) = -\sin\theta(\cos\theta\cos 2\phi\sin\psi + \sin 2\phi\cos\psi), \quad (16)$$

[4]One should note that there exist two different conventions of $\boldsymbol{e}^\ell(\hat{\mathbf{\Omega}})$ [80,81], and we adopt that of Callister *et al.* in Ref. [81] to follow their formalism consistently.

in terms of Euler angles on the detector frame, similar to Eqs. (7) and (8).

Since we assume unpolarized GW power within each of the vector and scalar polarizations similarly to the tensor polarizations, the pixel-based ORF for the nontensorial polarizations takes the same form as Eq. (2). Instead of the analytical expression described in Ref. [91], we follow the numerical approach shown in Refs. [95,96]. First, we substitute the polarization tensors shown in Eqs. (10)–(13) into Eq. (3) respectively to compute the pixel-based ORF with respect to the HealPix pixelization of $n_{\rm side} = 16$ (i.e. $12 \times 16^2 = 3072$ pixels) [97]. Subsequently, following Eq. (9), we convert it from the pixel basis to the SPH basis using the HEALPY package [98].

We note that, in the coordinate system where its z-axis points toward the Earth's rotational axis, the time dependence of the ORF due to the Earth's rotation is equivalent to the change in the azimuthal angle, and hence

$$\gamma^I_{\ell m}(f,t) = \gamma^I_{\ell m}(f,t_{\rm ref}) e^{im2\pi(t-t_{\rm ref})/T}, \tag{17}$$

where T is the period of the Earth's rotation. This factorization allows us to compute the SPH-based ORF at a reference time $\gamma^I_{\ell m}(f,t_{\rm ref})$ and the time-dependent phase separately. Eventually, $\gamma^I_{\ell m}(f,t_{\rm ref})$ is then multiplied by the phase factor to account for the proper time shift and to construct a two-dimensional f-t map, which substantially reduces the computational cost.

We show the SPH-based ORF of the two LIGO detector pair for each polarization family over 0 Hz to 500 Hz, e.g. for brevity only $(\ell, m) = (1, 1)$ and $(2, 2)$ modes in Figs. 1 and 2, respectively. Since the SPH-based ORF is a complex function in general, the left plot in either figure shows the real part of each $\gamma^I_{\ell m}(f,t_{\rm ref})$ and the right plot shows its imaginary part. Note that $t_{\rm ref}$ is adjusted such that the imaginary part of the tensorial ORF at $f = 0$ Hz is zero, which allows for a fair comparison of the plotted values across the three polarizations at the consistent reference time.

As mentioned in Sec. II A, at each frequency bin the amplitude of $\gamma^I_{\ell m}(f,t_{\rm ref})$ the sensitivity of the baseline I to the SGWB component whose spatial scale is characterized by the (ℓ, m) mode. The frequency range that yields the peaked amplitude is a consequence of the interplay between the diffraction effect in an observed SGWB signal and the phase canceling between two detectors at higher

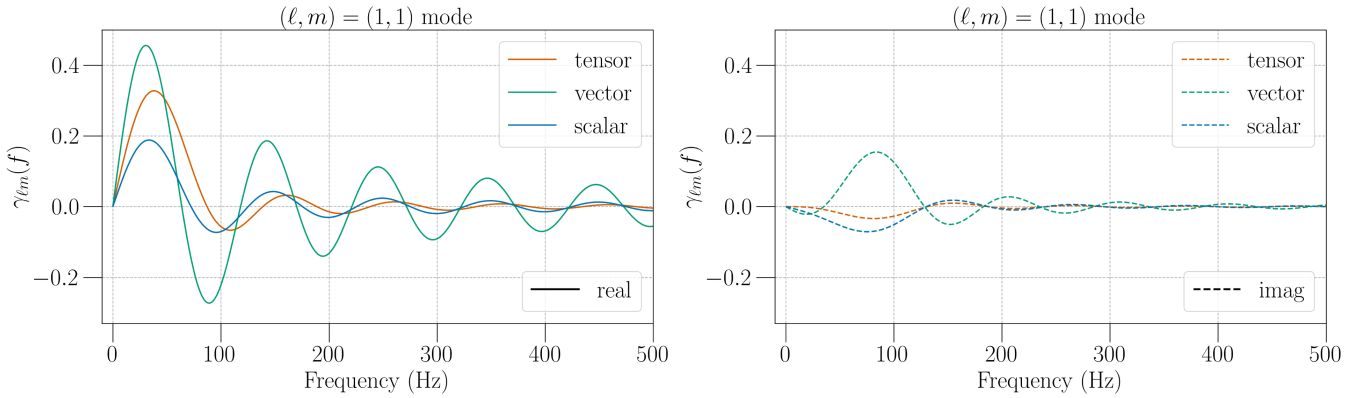

FIG. 1. SPH-based ORF of the two LIGO detector pair for each polarization family over 0 Hz to 500 Hz for $(\ell, m) = (1, 1)$ mode. The left plot shows the real part of the ORF, while the right one shows its imaginary part.

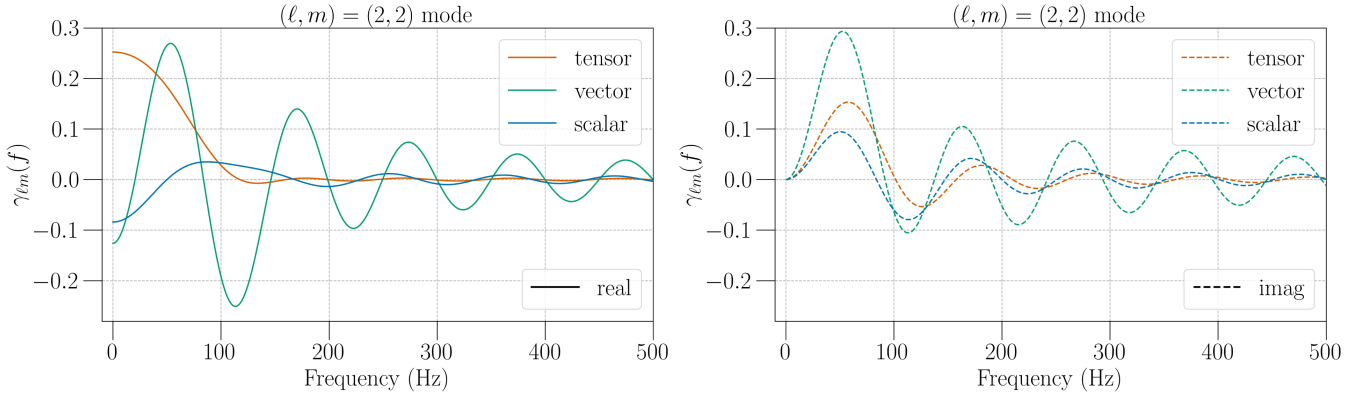

FIG. 2. SPH-based ORF of the two LIGO detector pair for each polarization family over 0 Hz to 500 Hz for $(\ell, m) = (2, 2)$ mode. The left plot shows the real part of the ORF, while the right one shows its imaginary part.

frequencies. As opposed to the diffraction limit suppressing sensitivity over lower frequencies, the signal components at higher frequencies tend to have phases at two detectors canceled out to some extent when taking crosscorrelation, leading to a decaying function of the ORF in general. This tradeoff is more noticeable for higher (ℓ, m) modes, e.g. Appendix A showing the ORF for $(\ell, m) = (10, 10)$ mode, which has the amplitude peaked at around 200 Hz.

III. BAYESIAN FORMALISM

A. Likelihood

Following the Bayesian formalism for an anisotropic SGWB discussed in Ref. [89], here we expand this approach to allow for an inferred signal model with nontensorial GW polarizations or even a mixture of different polarizations. In general, the mixture model of multiple signal components takes the form of

$$\sum_i \bar{H}_i(f)\gamma_\mu^{A_i}(f,t)\mathcal{P}_\mu^i, \tag{18}$$

where for i th signal component $\bar{H}^i(f;\boldsymbol{\theta}')$ is the frequency spectrum normalized at some reference frequency, A_i is its GW polarization and the subscript μ implies the summation over the SPH basis

$$\gamma_\mu^{A_i}(f,t)\mathcal{P}_\mu^i = \sum_{\ell=0}^{\ell_{\max,i}} \sum_{m=-\ell}^{\ell} \gamma_{\ell m}^{A_i}(f,t)\mathcal{P}_{\ell m}^i. \tag{19}$$

Note that in general the $\ell_{\max}$ value, i.e. spatial cutoff scale in the SPH expansion, can be different across signal components.

Following the approach described by Ref. [89], we normalize the $\mathcal{P}_{\ell m}$ such that

$$\mathcal{P}_{\ell m} = \epsilon\bar{\mathcal{P}}_{\ell m} \quad \text{s.t. } \bar{\mathcal{P}}_{00} = \frac{3H_0^2}{2\pi f_{\rm ref}^3\sqrt{4\pi}} \tag{20}$$

where ϵ is an amplitude parameter compatible to $\Omega_{\rm ref}$ in the conventional isotropic SGWB searches [83,84,99]. Henceforth, we consider $\bar{\mathcal{P}}_{\ell m}$ to be fixed for each signal component but still be potentially different across them. Given the multiple signal components $\boldsymbol{\mathcal{M}}$, each of which is characterized by $\bar{H}$, γ_μ and $\bar{\mathcal{P}}_\mu$, the Gaussian likelihood reads

$$p(\{C_{ft}\}|\{\epsilon_i,\boldsymbol{\theta}_i'\};\boldsymbol{\mathcal{M}}) \propto \exp\left\{-\frac{1}{2}\sum_{f,t}\frac{|C(f,t)-\sum_i\epsilon_i\bar{H}_i(f;\boldsymbol{\theta}_i')\gamma_\mu^{A_i}(f,t)\bar{\mathcal{P}}_\mu^i|^2}{P_1(f,t)P_2(f,t)}\right\}. \tag{21}$$

Here, $P_k(f,t)$ is the power spectral density (PSD) of k th detector, and $\boldsymbol{\theta}_i', \epsilon_i$ are a set of model parameters regarding $\bar{H}(f)$ and the amplitude parameter of the ith signal component in $\boldsymbol{\mathcal{M}}$, respectively. $\sum_i$ represents the summation across $\boldsymbol{\mathcal{M}}$. Note that the case of $\ell_{\max} = 0$ for all the signal components reduces to the isotropic search for nontensorial GW polarizations, e.g. [81,82]. Once a distribution of likelihood based on Eq. (21) is constructed, it will be used to produce a posterior probability distribution $p(\{\epsilon_i,\boldsymbol{\theta}_i'\}|\{C_{ft}\};\boldsymbol{\mathcal{M}})$ based on the Bayes' theorem.

B. Odds ratio

The Bayesian formalism provides a statistical way to evaluate the preference of a particular hypothesis over another, so-called *odds ratio* defined as

$$\mathcal{O}_{\mathcal{H}_2}^{\mathcal{H}_1} = \frac{p(\mathcal{H}_1|\{C_{ft}\})}{p(\mathcal{H}_2|\{C_{ft}\})} = \frac{p(\{C_{ft}\}|\mathcal{H}_1)}{p(\{C_{ft}\}|\mathcal{H}_2)}\frac{\pi(\mathcal{H}_1)}{\pi(\mathcal{H}_2)}, \tag{22}$$

where $\mathcal{H}_1$ is the hypothesis of interest and $\mathcal{H}_2$ is another one to compare that against. $p(\{C_{ft}\}|\mathcal{H})$ is the Bayesian *evidence* given by

$$p(\{C_{ft}\}|\mathcal{H}) = \int \mathbf{d}\boldsymbol{\theta}\, p(\{C_{ft}\}|\boldsymbol{\theta};\mathcal{H})p(\boldsymbol{\theta}), \tag{23}$$

and $\pi(\boldsymbol{\theta}), \pi(\mathcal{H})$ are the prior probability for the model parameters $\boldsymbol{\theta}$ and a hypothesis $\mathcal{H}$, respectively.

In the context of detecting nontensorial GW polarizations, similarly to Refs. [81,82], we consider the two hypotheses:

(i) GR: only the tensor polarization family is present in the data,
(ii) NGR: either scalar or vector polarization family is present in the data.

Therefore, denoting $\mathcal{H}_A$ as a subhypothesis of a given combination (or either) of tensor (T), vector (V) and scalar (S) polarizations present in data, the GR hypothesis corresponds to $\mathcal{H}_T$, while the NGR hypothesis consists of $\{\mathcal{H}_{\rm S}, \mathcal{H}_{\rm V}, \mathcal{H}_{\rm TS}, \mathcal{H}_{\rm VS}, \mathcal{H}_{\rm TV}, \mathcal{H}_{\rm TVS}\}$. Accordingly, the odds ratio of the NGR hypothesis against the GR counterpart reads

$$\mathcal{O}_{\rm GR}^{\rm NGR} = \frac{\sum_{A\neq \rm T} p(\{C_{ft}\}|\mathcal{H}_A)\pi(\mathcal{H}_A)}{p(\{C_{ft}\}|\mathcal{H}_{\rm T})\pi(\mathcal{H}_{\rm T})} \tag{24}$$

$$= \sum_{A\neq T} \mathcal{O}_{\mathcal{H}_{\rm T}}^{\mathcal{H}_A}. \tag{25}$$

Here, we assign the prior probability equally to each subhypothesis, i.e.

$$\pi(\mathcal{H}_{\rm A}) = \frac{1}{7} \quad {}^\forall A \in \{\rm T, S, V, TS, VS, TV, TVS\}. \tag{26}$$

C. Implementation

It is computationally challenging to evaluate the likelihood naively based on Eq. (21) as it involves the integration over frequency and time as well as summation across the SPH modes across multiple signal components. Reference [89] provides an implementation to bypass part of the calculation by precomputing the time integration. Here, we follow this approach and account for extra complication due to the presence of multiple signal components. Specifically, after expanding the exponent of Eq. (21), the logarithmic likelihood contains the following terms

$$\sum_i \epsilon_i \mathrm{Re}[(\bar{\mathcal{P}}^i_\mu)^* X^i_\mu] - \frac{1}{2}\sum_{i,j}\epsilon_i\epsilon_j (\bar{\mathcal{P}}^i_\mu)^* \Gamma^{ij}_{\mu\nu}\bar{\mathcal{P}}^j_\nu. \tag{27}$$

Here, the dirty map X_μ is an observable given by CSD convolved with detectors' response function and spectrum model $H(f)$, and the Fisher matrix $\Gamma_{\mu\nu}$ is the covariance matrix of the dirty map. See its full derivation in Ref. [88].

We note that these quantities are now specific to each signal component as follows[5]

$$X^i_\mu = \sum_f \bar{H}^i \underbrace{\sum_t \frac{\tau\Delta f (\gamma^{A_i}_\mu)^* C_{ft}}{P_1 P_2}}_{\text{precomputed for } A_i}, \tag{28}$$

$$\Gamma^{ij}_{\mu\nu} = \sum_f \bar{H}^i \bar{H}^j \underbrace{\sum_t \frac{\tau\Delta f (\gamma^{A_i}_\mu)^* \gamma^{A_j}_\nu}{P_1 P_2}}_{\text{precomputed for } (A_i,A_j)}, \tag{29}$$

where τ is the time interval over which the Fourier transform is applied to a time series strain data and Δf is the frequency resolution of CSD. Therefore, the precomputed part in the dirty map (the Fisher matrix) needs to be stored for each (every combination) of the three GW polarizations, respectively. Subsequently, during the likelihood evaluation the precomputed part with the associated polarization(s) of a given signal component or a pair of those is retrieved and used to compute Eqs. (28) and (29). This implementation allows the analysis to explore arbitrary signal-model space with minimal computational cost.

In order to efficiently construct a posterior probability density function (PDF) over a multidimensional parameter space, the pipeline stochastically samples a set of model parameters defined in a given signal model. Every time a new sample is drawn, the dirty map and the Fisher matrix are constructed based on Eqs. (28) and (29) and eventually the likelihood shown in Eq. (21), is evaluated. This sampling process is repeated until the Bayesian evidence is computed with sufficient precision. Specifically, we adopt a nested-sampling algorithm DYNESTY [100], implemented in the BILBY package. [101,102].

[5]The dependency on f, t and $\boldsymbol{\theta}'$ is omitted for brevity.

TABLE I. Configurations of the injection campaign.

	Polarization		$\ell_{\max}$	
	Injection	Recovery	Injection	Recovery
Case 1	Scalar	Scalar	5	5
Case 2	Scalar	Scalar	5	0
Case 3	Tensor	Scalar	5	5
Case 4	N/A	Scalar	N/A	5

IV. SIGNAL IDENTIFICATION

References [81,89] show, as described in Sec. III B, that one can use the odds ratio to evaluate the statistical significance for a signal model of interest. Here, we study the capability of detecting a signal among the noise and, more importantly, identifying a signal from the NGR hypothesis as opposed to the GR counterpart. To this end, in order to follow the case studies performed in Ref. [81], in this section and hereafter we restrict ourselves to considering an anisotropic SGWB injection with only scalar or tensor polarization family, or its mixture, which is also motivated by scalar-tensor theories [103]. Yet, this can be extended to include vector polarizations and the results are not expected to change drastically.

A. Single polarization

We first perform an injection campaign using synthetic SGWB signals with either scalar or tensor polarization. Specifically, the $\bar{\mathcal{P}}_{\ell m}$ distribution is generated from the mock Galactic plane shown in Fig. 1 of Ref. [89] with $\ell_{\max} = 5$ and the power-law spectrum $\bar{H}(f;\boldsymbol{\theta}')$ with the index $\alpha = 2/3$. The amplitude factor is determined such that the isotropic component ($\ell_{\max} = 0$) of the signal can be recovered with the optimal SNR $= 5$, i.e. $\epsilon \approx 1.8\times10^{-8}$ (4.3×10^{-9}) for the scalar (tensor) polarization, respectively.[6] Our pipeline injects this signal into simulated noise CSD between the two LIGO detectors of a one-year observation with the design sensitivity [104], and recovers it with the scalar polarization and $\ell_{\max} = 0$ or 5. In addition to these injection runs, we also analyze simulated data without injections, recovered with scalar polarization and $\ell_{\max} = 5$. Table I summarizes four cases of the configuration. Regarding the prior PDF, a log-uniform distribution and a Gaussian distribution with zero mean and a standard deviation of 3.5 are used for ϵ and α, respectively.

An analysis for each case is repeated for 500 different realizations of the noise CSD and produces a distribution of the log odds ratio $\ln \mathcal{O}^{\mathrm{SIG}}_{\mathrm{N}}$. Note that throughout this work

[6]See Eq. (9) in Ref. [81] for the definition of the optimal SNR.

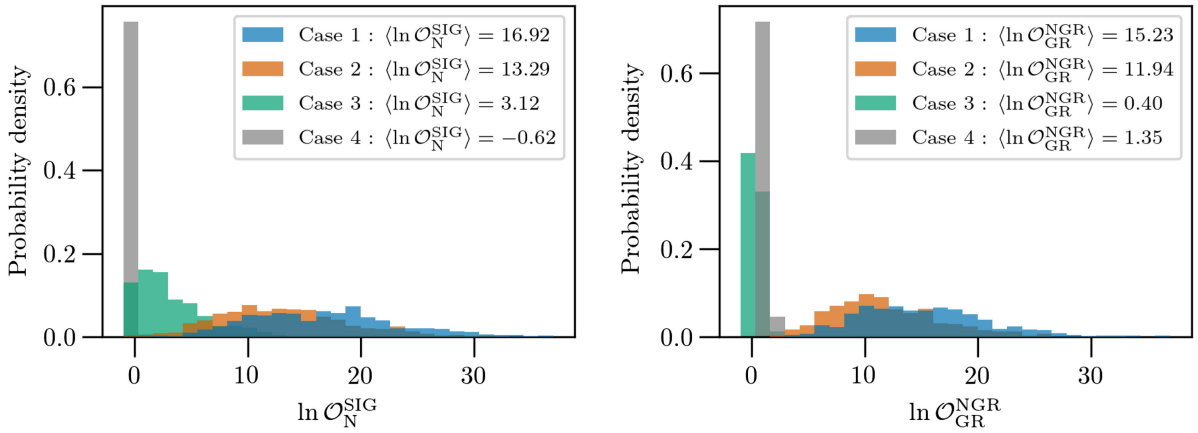

FIG. 3. Left: PDF of $\ln \mathcal{O}_{\rm N}^{\rm SIG}$ between signal and noise hypotheses for each of the four cases summarized in Table I. Right: PDF of $\ln \mathcal{O}_{\rm GR}^{\rm NGR}$ between the NGR and GR hypotheses for each of the four cases summarized in Table I.

the prior odds for both SIG and N models are assumed to be equal, and hence the odds ratio reduces to the Bayes factor,

$$\mathcal{B}_{\rm N}^{\rm SIG} = \frac{p(\{C_{ft}\}|{\rm SIG})}{p(\{C_{ft}\}|{\rm N})}. \tag{30}$$

The left plot in Fig. 3 shows a PDF of $\ln \mathcal{O}_{\rm N}^{\rm SIG}$ for each of the four cases represented by the different colors. One can see that the PDF for *Case 4* (the noninjection run) is narrowly distributed around zero, while those with the injections extend up to around $\ln \mathcal{O}_{\rm N}^{\rm SIG} = 30$. Even among these injection runs, the PDFs are largely distinct. In particular, the PDF of *Case 3* (with the injection of the tensor polarization) is strongly skewed toward zero and their mean is decreased from *Case 1* (recovered with the scalar polarization and) by more than 10 times, which suggests that the signal recovery using an inconsistent polarization reduces the capability of detecting the injected signal. Furthermore, apart from the composition of GW polarizations, the choice of $\ell_{\rm max} = 0$ (*Case 2*) or 5 (*Case 1*) makes a noticeable impact on the $\ln \mathcal{O}_{\rm N}^{\rm SIG}$ PDF. This is consistent with the results demonstrated in Ref. [89] despite the different GW polarization used for each study. More quantitatively speaking, the difference in the mean values of around 3.7 is in great agreement with the $\epsilon = 10^{-8}$ case of Fig. 8 therein. In summary, one can infer the $\ell_{\rm max}$ value as well as the GW polarization by comparing the $\ln \mathcal{O}_{\rm N}^{\rm SIG}$ computed by multiple signal models with the different choices of those hyperparameters. See a more thorough study in Sec. IV B.

Additionally, we analyze each realization of a dataset using the recovery signal model, which involves every possible polarization combination and is otherwise consistent with each of the four configurations listed in Table I. This allows us to calculate the odds ratio of the NGR hypothesis against the GR based on Eq. (24). Figure 3 indicates that overall the PDFs of $\ln \mathcal{O}_{\rm GR}^{\rm NGR}$ follows a similar behavior to those of $\ln \mathcal{O}_{\rm N}^{\rm SIG}$ except for *Case 3*. Therefore, the choice of $\ell_{\rm max}$ has a reasonable effect on not only signal detection but also a statistical test to assess the NGR hypothesis. Regarding the behavior of *Case 3*, despite the presence of the tensor polarization alone, the $\ln \mathcal{O}_{\rm GR}^{\rm NGR}$ does not strongly extend to a negative regime and its mean value is $\langle \ln \mathcal{O}_{\rm GR}^{\rm NGR} \rangle = 0.40$. This is because no detection of the nontensorial polarizations only places the upper limit of their SGWB amplitude and does *not* entirely prefer the GR hypothesis, being consistent with the statement in Ref. [81].

B. Mixed polarizations

To consider a more practical situation, we repeat the study described above using an SGWB injection with a mixture of the scalar and tensor polarizations. Following the configuration discussed in Ref. [81], for injected SGWB signals, we adopt the power-law $\bar{H}(f)$ spectrum with the power-law indices of $\alpha_T = 2/3$ and $\alpha_S = 0$. Throughout this study, the Galactic-plane $\bar{\mathcal{P}}_{\ell m}$ model is consistently used with $\ell_{\rm max} = 0(7)$ for the tensor (scalar) polarization, simulating a signal of an anisotropic scalar background overlying on top of an isotropic tensor background. We vary the amplitude factor for each polarization component such that $\log_{10} \epsilon_S$ ($\log_{10} \epsilon_T$) ranges from $-9.5(-10.0)$ to $-7.0(-7.5)$, and for a given grid point of the $\log_{10} \epsilon$ parameter space, a synthetic SGWB signal is injected into a realization of the noise data used in Sec. IV A. Also, injecting such a composite signal model complicates its implementation in terms of the precomputed parts, which is more discussed in Appendix B.

We analyze each dataset using the power-law $\bar{H}(f)+$ the Galactic-plane $\bar{\mathcal{P}}_{\ell m}$ model with every possible polarization combination to calculate $\ln \mathcal{O}_{\rm N}^{\rm SIG}$ and $\ln \mathcal{O}_{\rm GR}^{\rm NGR}$, adopting the same prior PDF for ϵ and α as in Sec. IV A. Eventually, a full set of runs produces a two-dimensional map of each quantity across the $\log_{10} \epsilon$ parameter space. This whole process is iterated for the two configurations of the

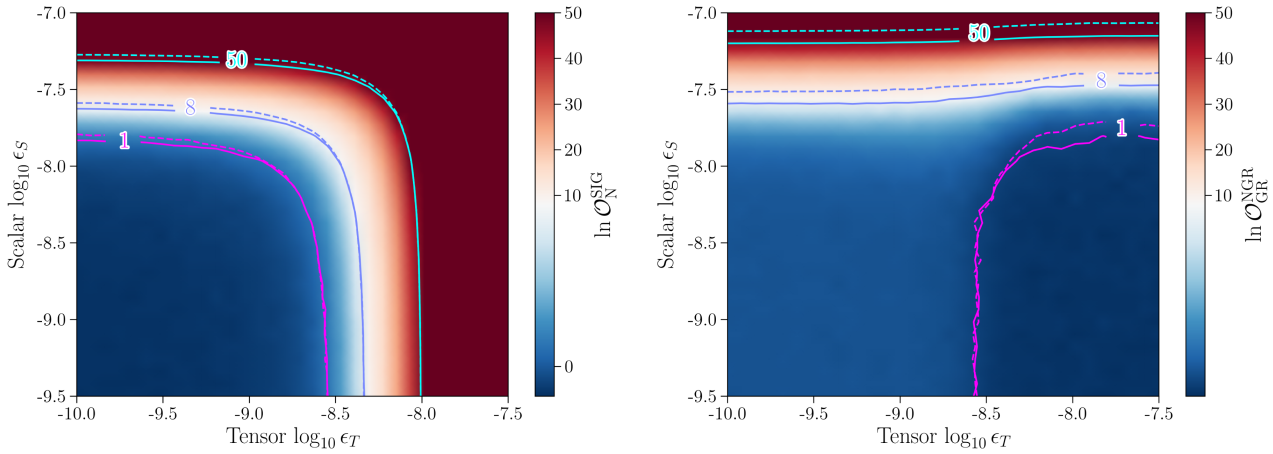

FIG. 4. Left: two-dimensional heat map of $\ln \mathcal{O}_{\rm N}^{\rm SIG}$ between signal and noise hypotheses with the solid (dashed) contours of $\ln \mathcal{O} = 1$, 8, 50 for *Case 1* (*Case 2*), respectively. Right: two-dimensional heat map of $\ln \mathcal{O}_{\rm GR}^{\rm NGR}$ between signal and noise hypotheses with the solid (dashed) contours of $\ln \mathcal{O} = 1$, 8, 50 for *Case 1* (*Case 2*), respectively.

recovery signal model as follows: For a given polarization combination,

(i) *Case 1*: $\ell_{\rm max} = 0$ for the tensor polarization and $\ell_{\rm max} = 7$ for the others,
(ii) *Case 2*: $\ell_{\rm max} = 0$ for both polarizations.

Figure 4 show a two-dimensional heat map of $\ln \mathcal{O}_{\rm N}^{\rm SIG}$ (left) and $\ln \mathcal{O}_{\rm GR}^{\rm NGR}$ (right) respectively for *Case 1* with solid contours of $\ln \mathcal{O} = 1$, 8, 50. As a comparison in both plots, a result for *Case 2* is represented by the dashed contours, each of which corresponds to the solid one with the same color. One can see that a larger ϵ_S yields greater $\ln \mathcal{O}_{\rm N}^{\rm SIG}$ or $\ln \mathcal{O}_{\rm GR}^{\rm NGR}$ and that, more importantly, the contours of *Case 2* (solid) all shift slightly below those of *Case 1* (dashed). This indicates that at a given (ϵ_T, ϵ_S) point, $\ln \mathcal{O}_{\rm N}^{\rm SIG}$ and $\ln \mathcal{O}_{\rm GR}^{\rm NGR}$ both increase by incorporating higher SPH modes of a scalar background into the recovery signal model. Regarding the ϵ_T dependency, $\ln \mathcal{O}_{\rm N}^{\rm SIG}$ monotonically increases with ϵ_T, while $\ln \mathcal{O}_{\rm GR}^{\rm NGR}$ rather decreases especially in the lower ϵ_S regime as the tensor polarization component in the injected signal starts to dominate over the scalar one. Although this overall structure of the two plots simply reproduces the results shown in Ref. [81], the key result here is the difference between *Case 1* and *Case 2*, which is also consistent with the behavior discussed in Fig. 3.

V. PARAMETER ESTIMATION

Apart from the signal detection evaluated by the odds ratio in the previous sections, parameter estimation is one of the meaningful products obtained by the Bayesian analysis, enriching the scientific implication. In this section, we study the behavior of posterior distributions with and without an anisotropic SGWB injection, using different configurations for the choice of the $\ell_{\rm max}$ values in recovery (e.g. $\ell_{\rm max} = 0$ or 7) as well as a detector network. Note that in the case of $\ell_{\rm max} = 0$ our formalism reduces to the Bayesian analysis for an isotropic SGWB, and hence this demonstrates a comparison between isotropic and anisotropic analyses. Throughout this study, we use a realization of the same dataset as Sec. IV A, where an SGWB signal synthesized from one or mixed GW polarizations may be present. For signal recovery, following Refs. [81,82], we adopt the most agnostic model in terms of the GW polarizations, i.e. $\mathcal{H}_{\rm TVS}$. Every polarization component of any signal model in this study involves the Galactic-plane $\bar{\mathcal{P}}_{\ell \rm m}$ (denoted as $\bar{\mathcal{P}}_{\mu}^{\rm GP}$) and a power-law $\bar{H}(f;\boldsymbol{\theta}')$ distribution, and hence the injection and recovery signal models both take the form of

$$\sum_A \epsilon_A \left(\frac{f}{25\ \rm Hz}\right)^{\alpha_A} \gamma_\mu^A(f,t)\bar{\mathcal{P}}_\mu^{\rm GP}. \tag{31}$$

Here, A indexes a GW polarization and runs across a set of those involved in a given signal model. Per GW polarization component, we take ϵ_A and α_A as free parameters to infer, which results in a joint posterior PDF concerning the six parameters in total. Throughout this study, we adopt the same prior PDF for ϵ_A and α_A as in Sec. IV A

A. Gaussian-noise test

We first consider a situation where no SGWB signal is present in a dataset of the two LIGO detectors and Virgo (HLV). This analysis yields $\ln \mathcal{O}_{\rm N}^{\rm SIG} = -2.05(-2.14)$ and $\ln \mathcal{O}_{\rm GR}^{\rm NGR} = 1.34(1.26)$ for $\ell_{\rm max} = 0(7)$, suggesting a non-detection of an SGWB signal. Figure 5 shows a joint posterior PDF of the analysis with $\ell_{\rm max} = 0$ (blue) and 7 (yellow) respectively, as well as a prior PDF (gray dotted) mentioned earlier. One can observe that the overall structure of the two posterior PDFs is largely consistent. Also, across all the polarizations extremely larger values of α are

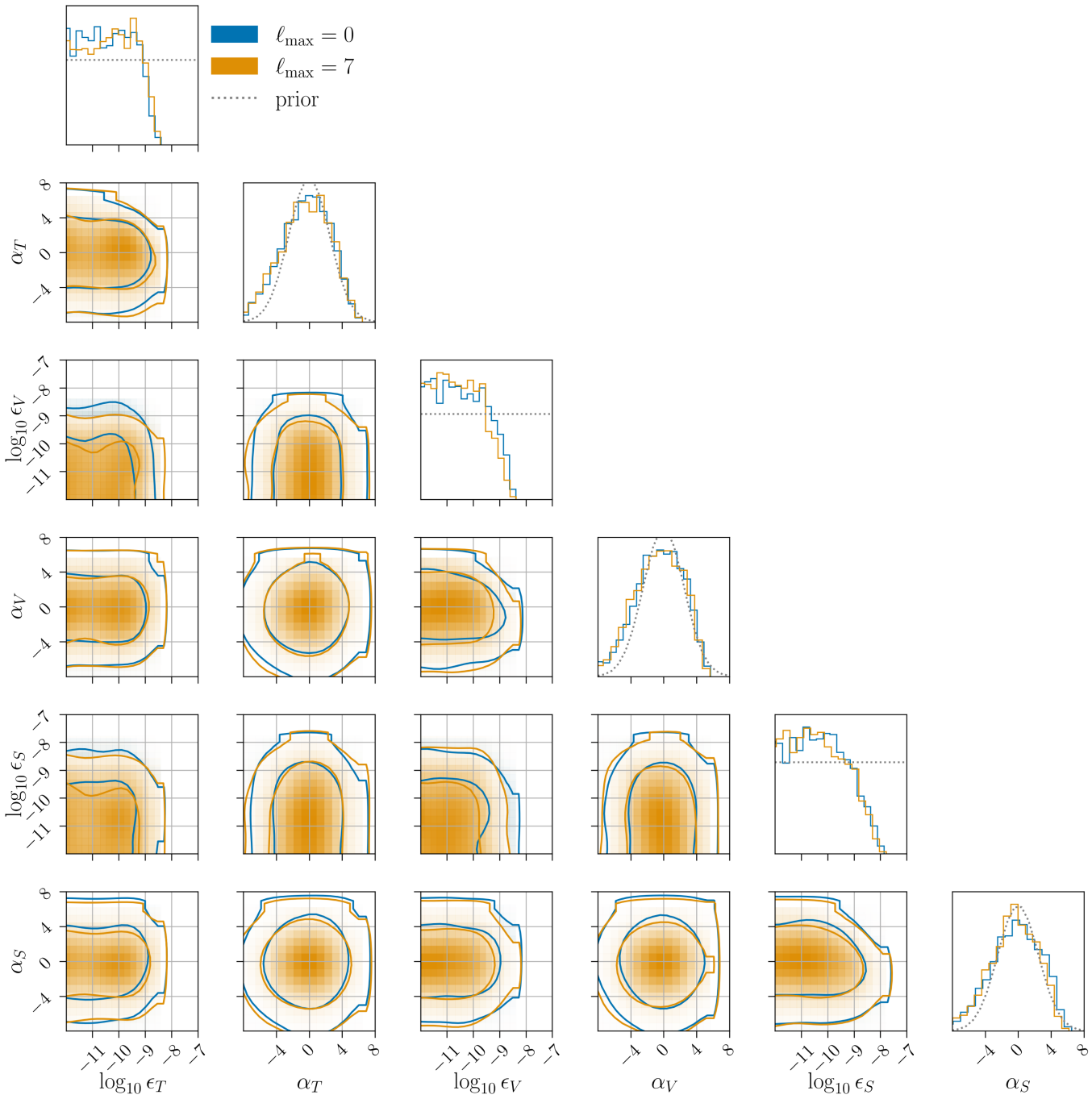

FIG. 5. Joint posterior PDF of the Gaussian noise test using the HLV dataset analyzed with $\ell_{\rm max} = 0$ (blue) and 7 (yellow) respectively, as well as a prior PDF (gray dotted) mentioned earlier. The model parameters to infer in $\mathcal{H}_{\rm TVS}$ hypothesis consist of the amplitude factor ϵ and the power-law index α for each polarization (e.g. tensor, vector, scalar from left to right in the x-axes).

TABLE II. 95% upper limits on the amplitude factor ϵ for each GW polarization obtained from the Gaussian noise test after marginalizing over the rest of the parameters.

	Tensor (ϵ_T)	Vector (ϵ_V)	Scalar (ϵ_S)
$\ell_{\rm max} = 0$	8.8×10^{-10}	1.0×10^{-9}	2.0×10^{-9}
$\ell_{\rm max} = 7$	1.0×10^{-9}	6.7×10^{-10}	1.8×10^{-9}

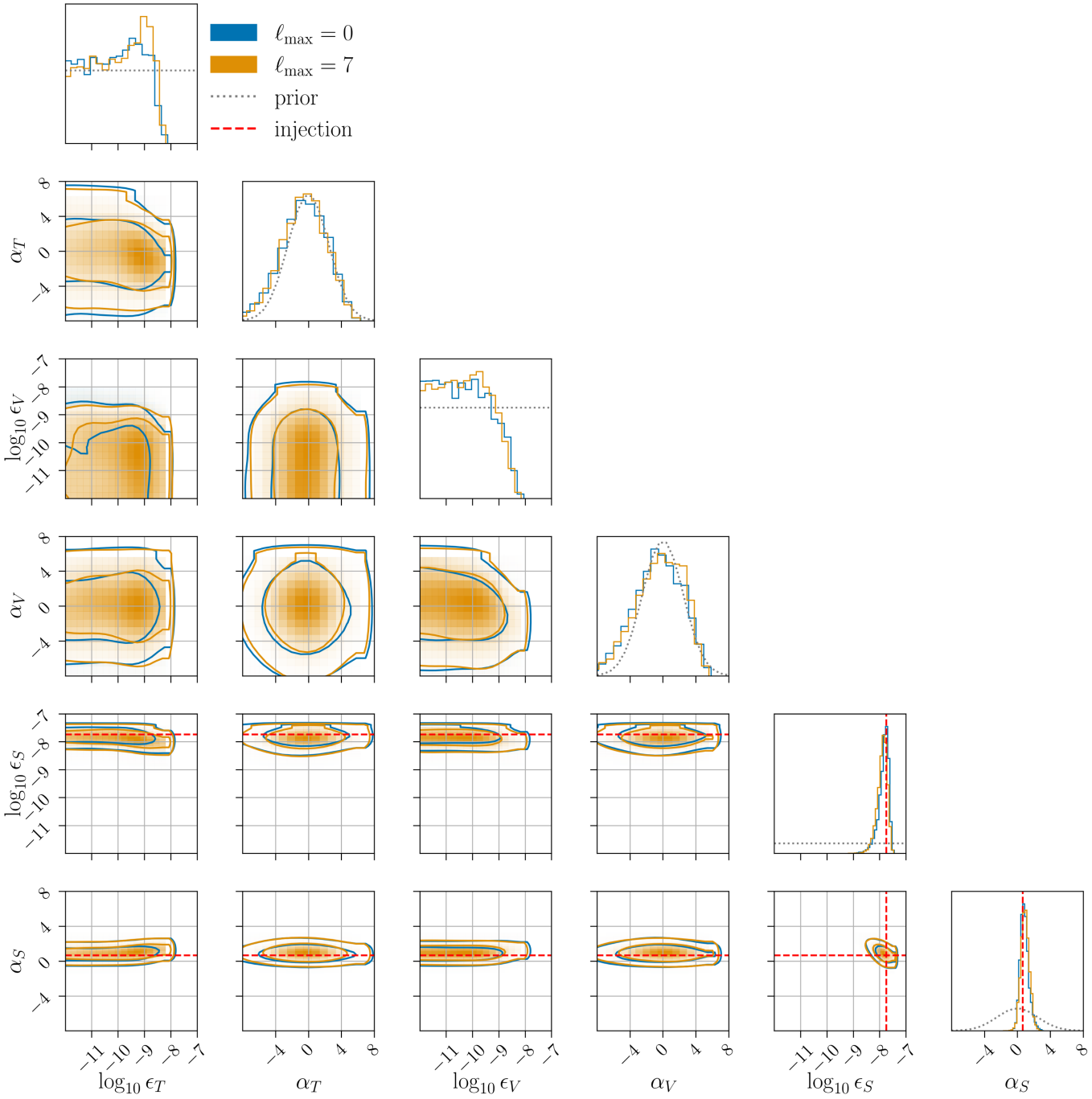

FIG. 6. Joint posterior PDF of the scalar injection test using the HLV dataset analyzed with $\ell_{\rm max} = 0$ (blue) and 7 (yellow) respectively, as well as a prior PDF (gray dotted) mentioned earlier. The model parameters to infer in $\mathcal{H}_{\rm TVS}$ hypothesis consist of the amplitude factor ϵ and the power-law index α for each polarization (e.g. tensor, vector, scalar from left to right in the x-axes).

TABLE III. $\ln \mathcal{O}^{\rm SIG}_{\rm N}$ and $\ln \mathcal{O}^{\rm NGR}_{\rm GR}$ obtained by the scalar injection test for each recovery $\ell_{\rm max}$ and detector network.

	$\ell_{\rm max} = 0$		$\ell_{\rm max} = 7$	
	HL	HLV	HL	HLV
$\ln \mathcal{O}^{\rm SIG}_{\rm N}$	12.49	15.35	13.65	16.02
$\ln \mathcal{O}^{\rm NGR}_{\rm GR}$	11.33	15.20	12.51	15.75

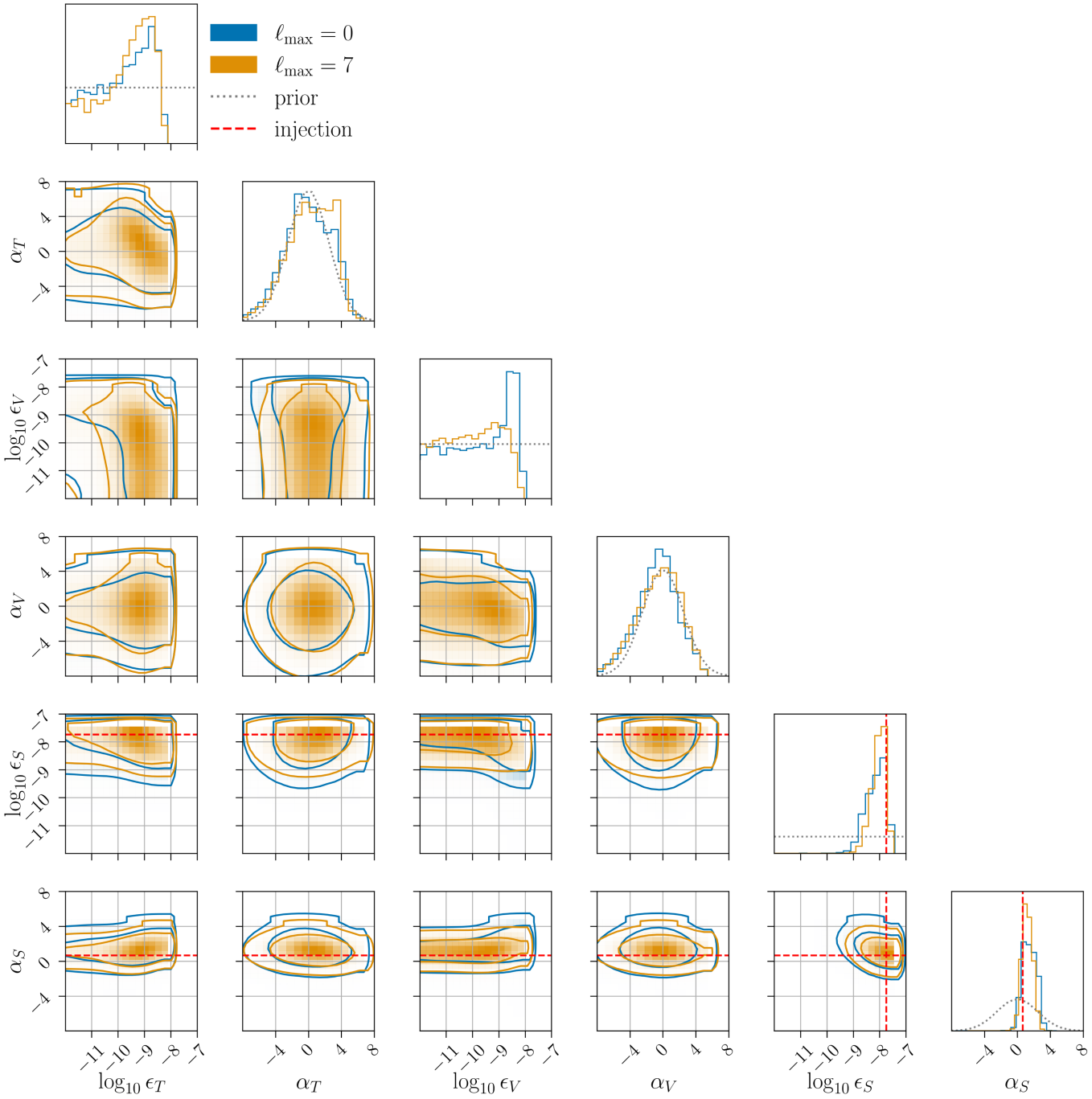

FIG. 7. Joint posterior PDF of the scalar injection test using the HL dataset analyzed with $\ell_{\max} = 0$ (blue) and 7 (yellow) respectively, as well as a prior PDF (gray dotted) mentioned earlier. The model parameters to infer in $\mathcal{H}_{\rm TVS}$ hypothesis consist of the amplitude factor ϵ and the power-law index α for each polarization (e.g. tensor, vector, scalar from left to right in the x-axes).

less likely than the smaller values because a frequency spectrum with such a steep slope would have been detected if exists. The null results of each run place an upper limit on the amplitude factor, ϵ, which is summarized in Table II. We note that although the upper limits derived from the two analyses vary by around $\mathcal{O}(10)\%$, these values should not be compared quantitatively as they are conceptually different searches, targeting isotropy or Galactic-place structure.

B. Single polarization injection

At this step, we simulate an anisotropic SGWB signal with the scalar polarization, adopting the power-law $\bar{H}(f)$ and the Galactic-plane $\bar{\mathcal{P}}_{\ell m}$ model with $\ell_{\max} = 7$. Similar to the injected signals described in Sec. IV A, the power-law index α_S is set to 2/3 and the amplitude factor is adjusted so that the isotropic component of the signal can be recovered with the optimal SNR = 5 for the given dataset,

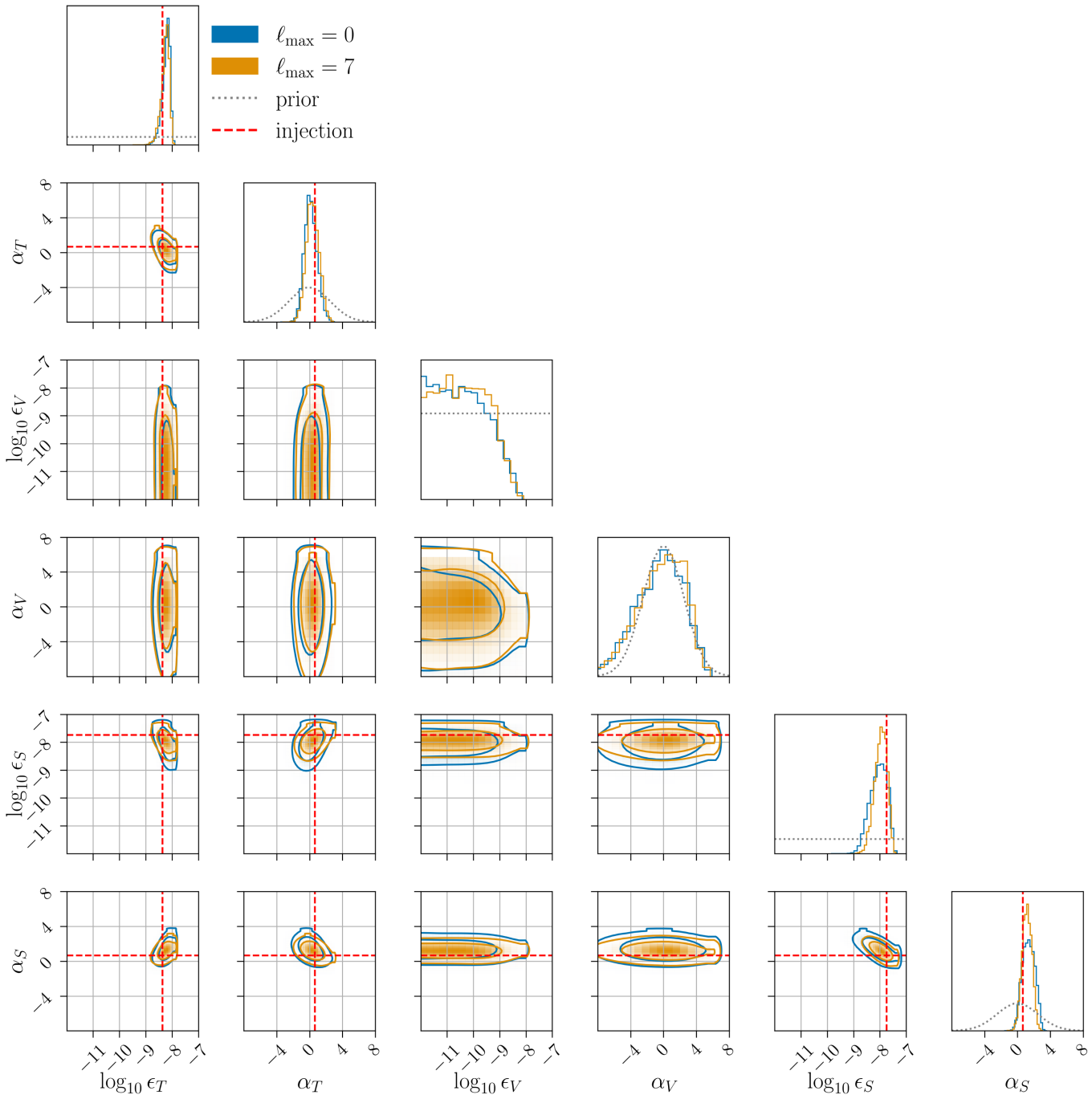

FIG. 8. Joint posterior PDF of the scalar-tensor mixed injection test using the HLV dataset analyzed with $\ell_{\rm max} = 0$ (blue) and 7 (yellow) respectively, as well as a prior PDF (gray dotted) mentioned earlier. The model parameters to infer in $\mathcal{H}_{\rm TVS}$ hypothesis consist of the amplitude factor ϵ and the power-law index α for each polarization (e.g. tensor, vector, scalar from left to right in the x-axes).

TABLE IV. $\ln \mathcal{O}^{\rm SIG}_{\rm N}$ and $\ln \mathcal{O}^{\rm NGR}_{\rm GR}$ obtained by the scalar-tensor mixed injection test for each recovery $\ell_{\rm max}$ and detector network.

	$\ell_{\rm max} = 0$		$\ell_{\rm max} = 7$	
	HL	HLV	HL	HLV
$\ln \mathcal{O}^{\rm SIG}_{\rm N}$	42.22	43.95	45.62	47.45
$\ln \mathcal{O}^{\rm NGR}_{\rm GR}$	10.27	12.38	13.50	15.75

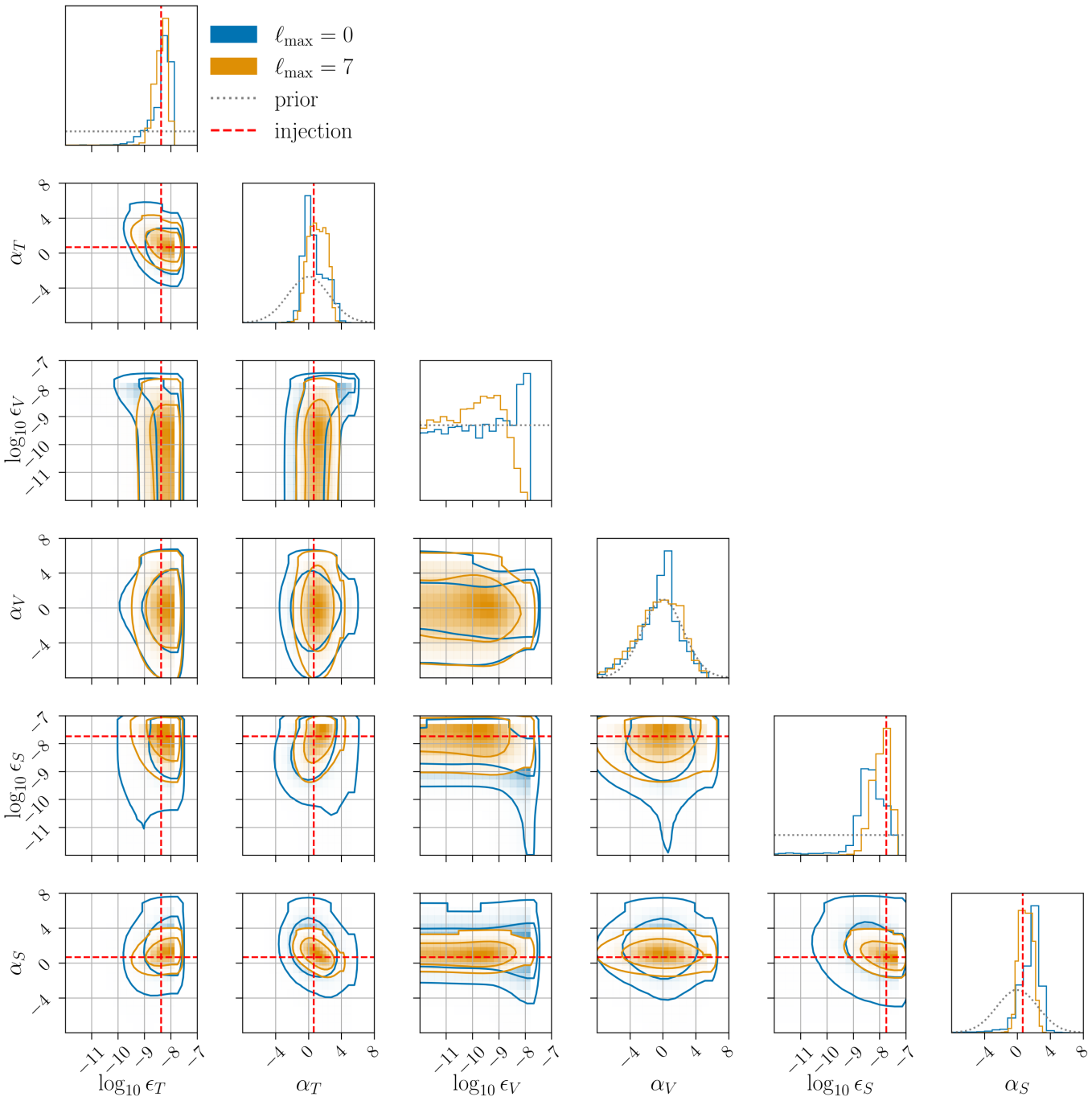

FIG. 9. Joint posterior PDF of the scalar-tensor mixed injection test using the HL dataset analyzed with $\ell_{\max} = 0$ (blue) and 7 (yellow) respectively, as well as a prior PDF (gray dotted) mentioned earlier. The model parameters to infer in $\mathcal{H}_{\rm TVS}$ hypothesis consist of the amplitude factor ϵ and the power-law index α for each polarization (e.g. tensor, vector, scalar from left to right in the x-axes).

e.g. $\epsilon_S \approx 1.8 \times 10^{-8}$. Analyzing the same HLV dataset as the Gaussian-noise test in the presence of such an SGWB injection, we obtain $\ln \mathcal{O}^{\rm SIG}_{\rm N}$ and $\ln \mathcal{O}^{\rm NGR}_{\rm GR}$ summarized in Tab. III for each $\ell_{\max}$ value. Both odds ratios indicate a great statistical significance and even increase for the $\ell_{\max} = 7$ case by around 3, which is consistent with Fig. 3. This implies that an analysis using $\mathcal{H}_{\rm TVS}$ hypothesis can properly obtain additional information from higher SPH modes imprinted in the data. Figure 6 shows posterior PDFs for each $\ell_{\max} = 0, 7$ case with the prior PDF and the injected value (red dashed) overlaid. Both analyses consistently recover the injected (ϵ_S, α_S) values and the overall structure of the two PDFs are in great agreement.

As a comparison, we repeat this study using a dataset of the two LIGO detectors (HL) with the same duration and sensitivity curve, which results in decreasing $\ln \mathcal{O}^{\rm SIG}_{\rm N}$,

$\ln \mathcal{O}^{\rm NGR}_{\rm GR}$ consistently for both $\ell_{\rm max}$ values (see Table III). Therefore, for the given dataset the addition of Virgo helps the pipeline to better identify the signal and distinguish between the NGR and GR hypotheses. Similar to Fig. 7, the results of posterior PDFs given by this HL dataset are shown in Fig. 6. One of the noticeable features compared to Fig. 7 is the poor precision of recovered (ϵ_S, α_S) PDF, which further supports the gain from the Virgo's data. Also, there exist apparent peaks in the PDFs of ϵ_T and ϵ_V, which reproduces the degeneracy between GW polarizations described in Ref. [81].

Regarding the anisotropic component of the signal, one can evaluate its detectability by comparing $\ln \mathcal{O}^{\rm SIG}_{\rm N}$ between $\ell_{\rm max} = 7$ and 0, namely

$$\ln \mathcal{O}^{\ell=7}_{\ell=0} = \ln \mathcal{O}^{\rm SIG}_{\rm N}|_{\ell=7} - \ln \mathcal{O}^{\rm SIG}_{\rm N}|_{\ell=0}. \tag{32}$$

According to Table III, $\ln \mathcal{O}^{\ell=7}_{\ell=0} = 1.16$ and 0.67 for HL and HLV dataset respectively, which does not indicate strong evidence of the anisotropic components given an expected SNR of the injected signal. Nevertheless, it is worth noting that the $\ell_{\rm max} = 7$ case mitigates the peak in ϵ_V's PDF. This can be understood by the fact that additional SPH modes lead to characteristic ORFs differing across GW polarizations in a signal model and provide extra consistency checks. In consequence, the precision of (ϵ_S, α_S) recovery slightly improves compared to the $\ell_{\rm max} = 0$ case.

C. Mixed polarization injection

Lastly, we further complicate a situation by mixing the scalar and tensor polarizations in the injected signal model. Following the injection model in Sec. V B, we consistently use the power-law $\bar{H}(f)$ and the Galactic-plane $\bar{\mathcal{P}}_{\ell m}$ model with $\ell_{\rm max} = 7$ for the *both* polarization components. Also, for each component, the power-law index is set to $2/3$ and the amplitude factor is adjusted so that the isotropic component of the signal can be recovered with the optimal SNR $= 5$ for the given dataset, i.e. $\epsilon_S \approx 1.8 \times 10^{-8}$ and $\epsilon_T \approx 4.3 \times 10^{-9}$. With this signal injected into the HLV dataset, Table IV shows that $\ln \mathcal{O}^{\rm SIG}_{\rm N}$ is significantly larger than those in Table III for both $\ell_{\rm max} = 0$ and 7 cases due to an additional polarization component in the injection, whereas $\ln \mathcal{O}^{\rm NGR}_{\rm GR}$ is largely consistent with Table III. Although, similar to Sec. V B, $\ln \mathcal{O}^{\ell=7}_{\ell=0}$ derived from Table IV (3.4 and 3.5 for HL and HLV dataset, respectively) does not show strong evidence of the anisotropic components, the posterior PDF shown in Fig. 8 indicates that a consistent recovery of the four injected parameters for both cases and that, for the PDFs of ϵ_S and α_S, the $\ell_{\rm max} = 7$ case produces slightly more precise estimates than the $\ell_{\rm max} = 0$ case.

The posterior PDFs derived from the HL dataset, as shown in Fig. 9, exhibits a rather outstanding difference between these cases. Specifically, the analysis with $\ell_{\rm max} = 7$ infers the injected parameter, ϵ_S and α_S in particular, more precisely than the $\ell_{\rm max} = 0$ case. Also, some of the parameters among different polarization components present degeneracies for the $\ell_{\rm max} = 0$ case, which is manifested as apparent peaks in ϵ_V and α_V's PDFs, whereas the $\ell_{\rm max} = 7$ case breaks the degeneracies and results in the more precise inference of these parameters. These findings, together with the injection studies in Sec. IV A and Sec. V B, indicate that in the presence of anisotropic SGWB signal the inclusion of higher SPH modes allows us not only to better identify signals but also to estimate signal parameters more precisely without severe degeneracy between them. Although in practice one does not know the right choice of $\ell_{\rm max}$ values *a priori*, Ref. [89] demonstrates a systematic way to optimize the choice of $\ell_{\rm max}$ values in terms of the odds ratio.

VI. CONCLUSION

In this work, we have described an extension of the Bayesian formalism searching for an anisotropic SGWB to incorporate nontensorial GW polarizations. In Sec. II A, we numerically compute the ORF for the scalar and vector polarizations on the SPH basis, $\gamma_{\ell m}(f)$, which encodes the sensitivity of a given detector pair to an anisotropic component of an SGWB characterized by the SPH's indices (ℓ, m). Adopting these ORFs, we generalize the likelihood function derived in Refs. [81,89] such that it allows for multiple components with different polarizations, $\bar{\mathcal{P}}_{\ell m}$ or $\bar{H}(f)$ in the recovery signal model.

To demonstrate the capability to detect a nontensorial anisotropic SGWB, we perform several simulation studies involving signal injections with one or a mixture of the GW polarizations. The results shown in Fig. 3 reproduce the findings discussed in Ref. [81] and further suggest that, compared to the $\ell_{\rm max} = 0$ case the right choice of the $\ell_{\rm max}$ value improves the detectability and the odd ratio of the NGR hypothesis, $\ln \mathcal{O}^{\rm NGR}_{\rm GR}$. We also examine the results of parameter estimation with regard to the $\mathcal{H}_{\rm TVS}$ hypothesis, using either HL or HLV dataset with and without an anisotropic SGWB injection. Similar to the previous injection study, we compare the posterior PDFs between the two cases of $\ell_{\rm max} = 7$ (the optimal value) and $\ell_{\rm max} = 0$ (the isotropic model). As a result, we find that, in the presence of an anisotropic SGWB, the addition of higher SPH modes into a recovery signal model helps to break the degeneracy among different polarization components even without Virgo's data and to infer model parameters more precisely.

In principle, the Bayesian formalism described in this work can be applied to any signal model. An example of an astrophysically motivated $\bar{\mathcal{P}}_{\ell m}$ distribution would be a population of millisecond pulsars in the Milky Way Galaxy, e.g. the $\bar{\mathcal{P}}_{\ell m}$ model developed in [105]. This formalism can

evaluate any non-GR polarization component originating from the population and, if it is sufficiently prominent, separate it from the GR component, as illustrated in Sec. V C. Practically speaking, however, one cannot adopt arbitrary large $\ell_{\max}$ value or a recovery signal model with numerous free parameters as those would make matrix computation or sampling process costly. Also, this formalism is intended to target a particular anisotropic distribution model by fixing $\bar{\mathcal{P}}_{\ell m}$ coefficients *a priori*, but ultimately we would be interested in directly inferring each of the coefficients and producing $\bar{\mathcal{P}}_{\ell m}$-independent results. At present, the $\bar{\mathcal{P}}_{\ell m}$ inference for physically meaningful $\ell_{\max}$ value is computationally infeasible for the same reason. One of the promising approaches to these issues might be to make use of a GPU during the likelihood evaluation, which may involve high-dimensional matrices. We leave this as a potential avenue for future improvement.

Alternatively, anisotropies subject to the cosmic variance, e.g. the large scale structure, are better suited to be modeled by not $\bar{\mathcal{P}}_{\ell m}$ distribution but the angular power spectrum, which is given by

$$C_\ell = \frac{1}{2\ell+1}\sum_m |\mathcal{P}_{\ell m}|^2. \tag{33}$$

Since the likelihood function for C_ℓ is highly nontrivial, the formalism for a C_ℓ-targeted search is not straightforward and has not been established yet, which remains to be future work to pursue. Despite these caveats, the formalism presented in this work has paved the way to establish a generalized Bayesian analysis for an SGWB including anisotropies and nontensorial polarizations.

ACKNOWLEDGMENTS

The author is grateful for computational resources provided by the LIGO Laboratory and supported by National Science Foundation Grants No. PHY-0757058 and No. PHY-0823459. This material is based upon work supported by NSF's LIGO Laboratory which is a major facility fully funded by the National Science Foundation. LIGO was constructed by the California Institute of Technology and Massachusetts Institute of Technology with funding from the National Science Foundation (NSF) and operates under cooperative agreement No. PHY-1764464. The author is supported by the National Science Foundation through Grants No. OAC-2103662 and No. PHY-2011865.

APPENDIX A: ORF ANALYSIS

As discussed in Sec. II A, the SPH-based ORF encodes the sensitivity of a given detector pair to an anisotropic component of an SGWB characterized by the SPH's indices (ℓ, m). This appendix is dedicated for further investigation and provides useful insight on its behavior across different detector pairs and (ℓ, m) modes.

Figures 10 and 11 show real and imaginary parts of the SPH-based ORF in $(\ell, m) = (1, 1)$ and (2, 2) modes, respectively, for the LIGO-Hanford and Virgo (HV) detector pair. Similar to the monopole ORF discussed in Ref. [81], the intervals between zeros are much shorter than those of HL detector pair shown in Figs. 1 and 2 because these intervals are disproportional to a separation between the two detectors. Also, over the whole frequency range, HV's ORFs are smaller than HL's by a factor of several, indicating that the geometry and orientation of the HV pair makes it less sensitive to those SPH modes.

In contrast, the ORF for $(\ell, m) = (10, 10)$ mode plotted in Figs. 12 and 13 show some promise for the HV pair with the following features. First, one can see that both HL and HV's ORFs have the global peak of their amplitude located far away from 0 Hz. This reflects the fact that a higher-frequency component of a given signal has a better spatial resolution of its source. Second, the peak location for HV's ORF is shifted slightly toward lower frequencies (∼100 Hz). This can be explained by the diffraction-limit

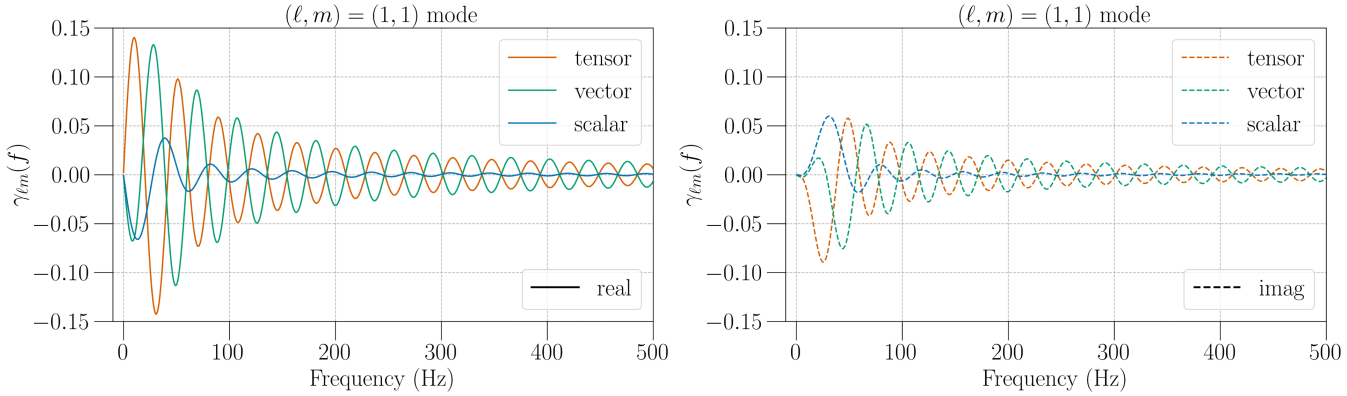

FIG. 10. SPH-based ORF of the LIGO-Hanford and Virgo detector pair for each polarization family over 0 Hz to 500 Hz for $(\ell, m) = (1, 1)$ mode. The left plot shows the real part of the ORF, while the right one shows its imaginary part.

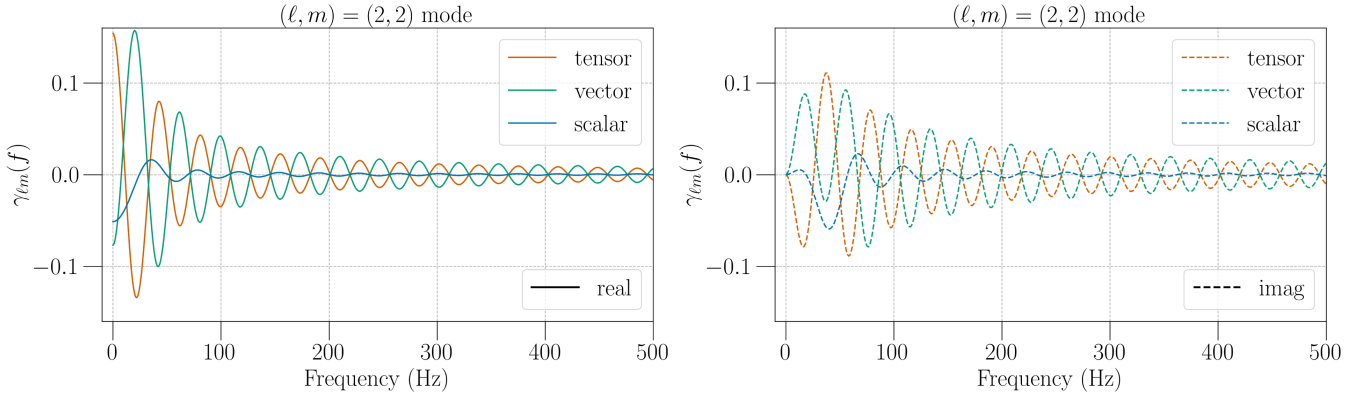

FIG. 11. SPH-based ORF of the LIGO-Hanford and Virgo detector pair for each polarization family over 0 Hz to 500 Hz for $(\ell, m) = (2, 2)$ mode. The left plot shows the real part of the ORF, while the right one shows its imaginary part.

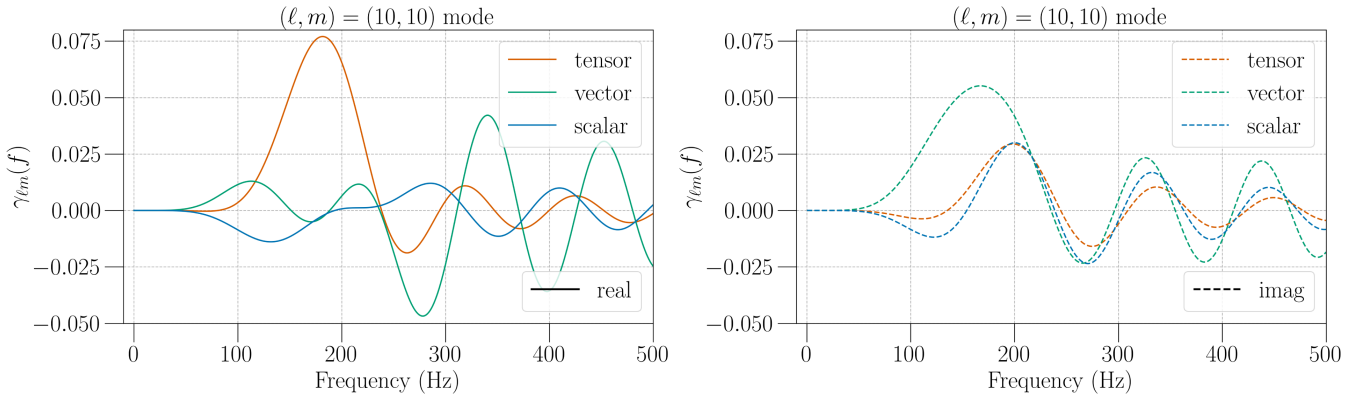

FIG. 12. SPH-based ORF of the two LIGO detector pair for each polarization family over 0 Hz to 500 Hz for $(\ell, m) = (10, 10)$ mode. The left plot shows the real part of the ORF, while the right one shows its imaginary part.

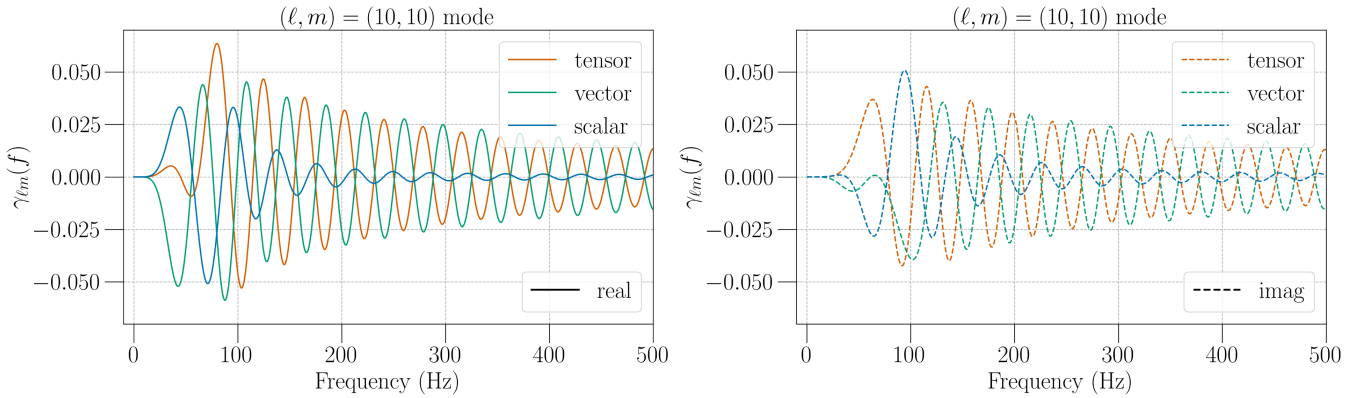

FIG. 13. SPH-based ORF of the LIGO-Hanford and Virgo detector pair for each polarization family over 0 Hz to 500 Hz for $(\ell, m) = (10, 10)$ mode. The left plot shows the real part of the ORF, while the right one shows its imaginary part.

argument discussed in the literature (e.g. [106–109]), where the angular resolution on the sky is determined by the separation between detectors (D) and the most sensitive frequency (f):

$$\theta = \frac{c}{2Df}. \tag{A1}$$

In other words, the typical frequencies sensitive to the given θ is disproportional to the separation. Third, most importantly, the overall amplitude of HV's ORF at around 100 Hz is larger than HL's, particularly for the scalar and vector polarizations. Although the diffraction-limit argument has qualitatively described this behavior, this investigation more clearly demonstrates the

advantage of the Virgo detector in terms of the sensitivity to an anisotropic SGWB. In reality, however, the overall sensitivity of a given detector pair should account for the PSD of each detector as well, which suppresses the benefit from HV's ORF given the current projection of Virgo's sensitivity.

APPENDIX B: INJECTING A COMPOSITE SIGNAL MODEL

Here we describe our implementation of SGWB injection on the frequency and SPH domain in the presence of multiple components in a signal model. To begin with, building upon Eq. (23) in Ref. [89], injecting such a composite signal model into CSD reads

$$C(f,t) = C_n(f,t) + \sum_a \epsilon_a^{\rm inj} \bar{H}_a^{\rm inj}(f;\{\vec{\theta}^{\rm inj}\})\gamma_\mu^{A_a}(f,t)\bar{\mathcal{P}}_\mu^{{\rm inj},a}, \tag{B1}$$

where $C_n(f,t)$ is *noise-only* CSD, the superscript $^{\rm inj}$ denotes each model or parameter intended for an injection and the index runs across all the components in a given signal model for injection. Substituting this expression into Eq. (21), the expansion of its exponent yields the following additional terms

$$-\sum_a \epsilon_a^{\rm inj}{\rm Re}[(\bar{\mathcal{P}}_\mu^{{\rm inj},a})^* X_\mu^{{\rm inj},a}] - \frac{1}{2}\sum_{a,b}\epsilon_a^{\rm inj}\epsilon_b^{\rm inj}(\bar{\mathcal{P}}_\mu^{{\rm inj},a})^*\Gamma_{\mu\nu}^{{\rm inj},ab}\bar{\mathcal{P}}_\nu^{{\rm inj},b} + \sum_{a,i}\epsilon_a^{\rm inj}\epsilon_i{\rm Re}[(\bar{\mathcal{P}}_\mu^{{\rm inj},a})^*\Gamma_{\mu\nu}^{(c),ai}\bar{\mathcal{P}}_\nu^i], \tag{B2}$$

due to the injection apart from the terms in Eq. (27) arising from the recovery signal model. In Eq. (B2), the indices (a,b) run across all the components in a given signal model for injection, while the index i denotes a component in a given signal model for recovery. $X_\mu^{{\rm inj},a}$ and $\Gamma_{\mu\nu}^{{\rm inj},ab}$ are based on similar definitions to those shown in Eqs. (28) and (29), respectively, replacing the indices (i,j) with (a,b) and C with C_n. Also, $\Gamma_{\mu\nu}^{(c),ai}$ is the *coupled* Fisher matrix defined as

$$\Gamma_{\mu\nu}^{(c),ai} = \sum_f\sum_t \gamma_\mu^{A_a *}(f,t)\frac{\tau\Delta f\bar{H}_i\bar{H}_a^{\rm inj}}{P_1(f,t)P_2(f,t)}\gamma_\nu^{A_i}(f,t), \tag{B3}$$

generalizing Eq. (25) in Ref. [89].

[1] B. Abbott, R. Abbott, T. Abbott, S. Abraham, F. Acernese, K. Ackley, C. Adams, R. Adhikari, V. Adya, C. Affeldt *et al.*, Gwtc-1: A gravitational-wave transient catalog of compact binary mergers observed by Ligo and Virgo during the first and second observing runs, Phys. Rev. X **9**, 031040 (2019).

[2] R. Abbott *et al.* (LIGO Scientific Collaboration and Virgo Collaboration), Gwtc-2: Compact binary coalescences observed by Ligo and Virgo during the first half of the third observing run, Phys. Rev. X **11**, 021053 (2021).

[3] R. Abbott *et al.* (The LIGO Scientific Collaboration and The Virgo Collaboration), Gwtc-2.1: Deep extended catalog of compact binary coalescences observed by LIGO and Virgo during the first half of the third observing run, arXiv:2108.01045.

[4] R. Abbott *et al.* (The LIGO Scientific Collaboration, The Virgo Collaboration, and The KAGRA Collaboration), Gwtc-3: Compact binary coalescences observed by LIGO and Virgo during the second part of the third observing run, arXiv:2111.03606.

[5] B. P. Abbott *et al.* (LIGO Scientific Collaboration and Virgo Collaboration), Observation of gravitational waves from a binary black hole merger, Phys. Rev. Lett. **116**, 061102 (2016).

[6] B. P. Abbott *et al.* (LIGO Scientific Collaboration and Virgo Collaboration), Gw151226: Observation of gravitational waves from a 22-solar-mass binary black hole coalescence, Phys. Rev. Lett. **116**, 241103 (2016).

[7] B. P. Abbott *et al.* (LIGO Scientific and Virgo Collaboration), Gw170104: Observation of a 50-solar-mass binary black hole coalescence at redshift 0.2, Phys. Rev. Lett. **118**, 221101 (2017).

[8] B. P. Abbott *et al.*, GW170608: Observation of a 19 solar-mass binary black hole coalescence, Astrophys. J. **851**, L35 (2017).

[9] B. P. Abbott *et al.* (LIGO Scientific Collaboration and Virgo Collaboration), Gw170814: A three-detector observation of gravitational waves from a binary black hole coalescence, Phys. Rev. Lett. **119**, 141101 (2017).

[10] R. Abbott *et al.* (LIGO Scientific and Virgo Collaborations), Gw190412: Observation of a binary-black-hole coalescence with asymmetric masses, Phys. Rev. D **102**, 043015 (2020).

[11] R. Abbott *et al.*, Gw190521: A binary black hole merger with a total mass of 150 solar mass, Phys. Rev. Lett. **125**, 101102 (2020).

[12] R. Abbott *et al.*, GW190814: Gravitational waves from the coalescence of a 23 solar mass black hole with a 2.6 solar mass compact object, Astrophys. J. Lett. **896**, L44 (2020).

[13] B. P. Abbott *et al.*, GW170817: Observation of gravitational waves from a binary neutron star inspiral, Phys. Rev. Lett. **119**, 161101 (2017).

[14] B. P. Abbott *et al.*, GW190425: Observation of a compact binary coalescence with total mass ~3.4 solar mass, Astrophys. J. Lett. **892**, L3 (2020).

[15] G. Agazie *et al.*, The nanograv 15 yr data set: Evidence for a gravitational-wave background, Astrophys. J. Lett. **951**, L8 (2023).
[16] D. J. Reardon *et al.*, Search for an isotropic gravitational-wave background with the Parkes pulsar timing array, Astrophys. J. Lett. **951**, L6 (2023).
[17] H. Xu *et al.*, Searching for the nano-hertz stochastic gravitational wave background with the chinese pulsar timing array data release I, Res. Astron. Astrophys. **23**, 075024 (2023).
[18] J. Antoniadis *et al.*, The second data release from the european pulsar timing array III. Search for gravitational wave signals, Astron. Astrophys. **678**, A50 (2023).
[19] A. I. Renzini, B. Goncharov, A. C. Jenkins, and P. M. Meyers, Stochastic gravitational-wave backgrounds: Current detection efforts and future prospects, Galaxies **10**, 34 (2022).
[20] M. Rajagopal and R. W. Romani, Ultra–low-frequency gravitational radiation from massive black hole binaries, Astrophys. J. **446**, 543 (1995).
[21] A. H. Jaffe and D. C. Backer, Gravitational waves probe the coalescence rate of massive black hole binaries, Astrophys. J. **583**, 616 (2003).
[22] J. S. B. Wyithe and A. Loeb, Low-frequency gravitational waves from massive black hole binaries: Predictions for lisa and pulsar timing arrays, Astrophys. J. **590**, 691 (2003).
[23] A. Sesana, F. Haardt, P. Madau, and M. Volonteri, Low-frequency gravitational radiation from coalescing massive black hole binaries in hierarchical cosmologies, Astrophys. J. **611**, 623 (2004).
[24] S. T. McWilliams, J. P. Ostriker, and F. Pretorius, Gravitational waves and stalled satellites from massive galaxy mergers at $z \leq 1$, Astrophys. J. **789**, 156 (2014).
[25] S. Burke-Spolaor, S. R. Taylor, M. Charisi, T. Dolch, J. S. Hazboun, A. M. Holgado, L. Z. Kelley, T. J. W. Lazio, D. R. Madison, N. McMann, C. M. F. Mingarelli, A. Rasskazov, X. Siemens, J. J. Simon, and T. L. Smith, The astrophysics of nanohertz gravitational waves, Astron. Astrophys. Rev. **27**, 5 (2019).
[26] T. Regimbau and V. Mandic, Astrophysical sources of a stochastic gravitational-wave background, Classical Quantum Gravity **25**, 184018 (2008).
[27] T. Regimbau, The quest for the astrophysical gravitational-wave background with terrestrial detectors, Symmetry **14**, 270 (2022).
[28] S. Banagiri, V. Mandic, C. Scarlata, and K. Z. Yang, Measuring angular N-point correlations of binary black hole merger gravitational-wave events with hierarchical Bayesian inference, Phys. Rev. D **102**, 063007 (2020).
[29] E. Payne, S. Banagiri, P. D. Lasky, and E. Thrane, Searching for anisotropy in the distribution of binary black hole mergers, Phys. Rev. D **102**, 102004 (2020).
[30] R. Stiskalek, J. Veitch, and C. Messenger, Are stellar-mass binary black hole mergers isotropically distributed?, Mon. Not. R. Astron. Soc. **501**, 970 (2020).
[31] S. Marassi, R. Schneider, and V. Ferrari, Gravitational wave backgrounds and the cosmic transition from Population III to Population II stars, Mon. Not. R. Ast. Soc. **398**, 293 (2009).
[32] X.-J. Zhu, E. Howell, and D. Blair, Observational upper limits on the gravitational wave production of core collapse supernovae, Mon. Not. R. Ast. Soc. **409**, L132 (2010).
[33] A. Buonanno, G. Sigl, G. G. Raffelt, H.-T. Janka, and E. Müller, Stochastic gravitational-wave background from cosmological supernovae, Phys. Rev. D **72**, 084001 (2005).
[34] P. Sandick, K. A. Olive, F. Daigne, and E. Vangioni, Gravitational waves from the first stars, Phys. Rev. D **73**, 104024 (2006).
[35] M. Cavaglià and A. Modi, Two-dimensional correlation function of binary black hole coalescences, Universe **6**, 93 (2020).
[36] R. Bar-Kana, Limits on direct detection of gravitational waves, Phys. Rev. D **50**, 1157 (1994).
[37] A. A. Starobinskiĭ, Spectrum of relict gravitational radiation and the early state of the universe, Sov. J. Exp. Theor. Phys. Lett. **30**, 682 (1979).
[38] R. Easther, J. T. Giblin, Jr., and E. A. Lim, Gravitational wave production at the end of inflation, Phys. Rev. Lett. **99**, 221301 (2007).
[39] N. Barnaby, E. Pajer, and M. Peloso, Gauge field production in axion inflation: Consequences for monodromy, non-Gaussianity in the CMB, and gravitational waves at interferometers, Phys. Rev. D **85**, 023525 (2012).
[40] J. L. Cook and L. Sorbo, Particle production during inflation and gravitational waves detectable by ground-based interferometers, Phys. Rev. D **85**, 023534 (2012).
[41] A. Lopez and K. Freese, First test of high frequency gravity waves from inflation using Advanced LIGO, J. Cosmol. Astropart. Phys. 01 (2015) 037.
[42] M. S. Turner, Detectability of inflation-produced gravitational waves, Phys. Rev. D **55**, R435 (1997).
[43] R. Easther and E. A. Lim, Stochastic gravitational wave production after inflation, J. Cosmol. Astropart. Phys. 04 (2006) 010.
[44] S. G. Crowder, R. Namba, V. Mandic, S. Mukohyama, and M. Peloso, Measurement of parity violation in the early universe using gravitational-wave detectors, Phys. Lett. B **726**, 66 (2013).
[45] B. Von Harling, A. Pomarol, O. Pujolàs, and F. Rompineve, Peccei-Quinn phase transition at LIGO, J. High Energy Phys. 04 (2020) 195.
[46] P. S. B. Dev and A. Mazumdar, Probing the scale of new physics by Advanced LIGO/VIRGO, Phys. Rev. D **93**, 104001 (2016).
[47] L. Marzola, A. Racioppi, and V. Vaskonen, Phase transition and gravitational wave phenomenology of scalar conformal extensions of the Standard Model, Eur. Phys. J. C **77**, 484 (2017).
[48] V. Mandic, S. Bird, and I. Cholis, Stochastic gravitational-wave background due to primordial binary black hole mergers, Phys. Rev. Lett. **117**, 201102 (2016).
[49] M. Sasaki, T. Suyama, T. Tanaka, and S. Yokoyama, Primordial black hole scenario for the gravitational-wave event GW150914, Phys. Rev. Lett. **117**, 061101 (2016).
[50] S. Wang, Y.-F. Wang, Q.-G. Huang, and T. G. F. Li, Constraints on the primordial black hole abundance from the first Advanced LIGO observation run using the

stochastic gravitational-wave background, Phys. Rev. Lett. **120**, 191102 (2018).
[51] A. L. Miller, S. Clesse, F. De Lillo, G. Bruno, A. Depasse, and A. Tanasijczuk, Probing planetary-mass primordial black holes with continuous gravitational waves, Phys. Dark Universe **32**, 100836 (2021).
[52] J. Aasi *et al.* (LIGO Scientific Collaboration), Advanced LIGO, Classical Quantum Gravity **32**, 074001 (2015).
[53] F. Acernese *et al.* (VIRGO Collaboration), Advanced Virgo: A second-generation interferometric gravitational wave detector, Classical Quantum Gravity **32**, 024001 (2015).
[54] T. Akutsu *et al.*, Overview of kagra: Detector design and construction history, Prog. Theor. Exp. Phys. **2021**, 05A101 (2021).
[55] B. P. Abbott *et al.* (LIGO Scientific and Virgo Collaborations), Tests of general relativity with GW150914, Phys. Rev. Lett. **116**, 221101 (2016).
[56] B. P. Abbott *et al.* (LIGO Scientific Collaboration and Virgo Collaboration), Tests of general relativity with GW170817, Phys. Rev. Lett. **123**, 011102 (2019).
[57] B. P. Abbott *et al.*, Tests of general relativity with the binary black hole signals from the LIGO-Virgo catalog gwtc-1, Phys. Rev. D **100**, 104036 (2019).
[58] R. Abbott *et al.*, Tests of general relativity with binary black holes from the second LIGO-Virgo gravitational-wave transient catalog, Phys. Rev. D **103**, 122002 (2021).
[59] R. Abbott *et al.* (The LIGO Scientific Collaboration, the Virgo Collaboration, and the KAGRA Collaboration), Tests of general relativity with gwtc-3, arXiv:2112.06861.
[60] L. Blanchet and B. S. Sathyaprakash, Signal analysis of gravitational wave tails, Classical Quantum Gravity **11**, 2807 (1994).
[61] L. Blanchet and B. S. Sathyaprakash, Detecting a tail effect in gravitational-wave experiments, Phys. Rev. Lett. **74**, 1067 (1995).
[62] K. G. Arun, B. R. Iyer, M. S. S. Qusailah, and B. S. Sathyaprakash, Testing post-Newtonian theory with gravitational wave observations, Classical Quantum Gravity **23**, L37 (2006).
[63] K. G. Arun, B. R. Iyer, M. S. S. Qusailah, and B. S. Sathyaprakash, Probing the nonlinear structure of general relativity with black hole binaries, Phys. Rev. D **74**, 024006 (2006).
[64] N. Yunes and F. Pretorius, Fundamental theoretical bias in gravitational wave astrophysics and the parametrized post-Einsteinian framework, Phys. Rev. D **80**, 122003 (2009).
[65] B. P. Abbott *et al.*, Gravitational waves and gamma-rays from a binary neutron star merger: GW170817 and GRB 170817a, Astrophys. J. **848**, L13 (2017).
[66] J. Healy and C. O. Lousto, Remnant of binary black-hole mergers: New simulations and peak luminosity studies, Phys. Rev. D **95**, 024037 (2017).
[67] F. Hofmann, E. Barausse, and L. Rezzolla, The final spin from binary black holes in quasi-circular orbits, Astrophys. J. Lett. **825**, L19 (2016).
[68] X. Jiménez-Forteza, D. Keitel, S. Husa, M. Hannam, S. Khan, and M. Pürrer, Hierarchical data-driven approach to fitting numerical relativity data for nonprecessing binary black holes with an application to final spin and radiated energy, Phys. Rev. D **95**, 064024 (2017).
[69] J. Westerweck, A. B. Nielsen, O. Fischer-Birnholtz, M. Cabero, C. Capano, T. Dent, B. Krishnan, G. Meadors, and A. H. Nitz, Low significance of evidence for black hole echoes in gravitational wave data, Phys. Rev. D **97**, 124037 (2018).
[70] N. Uchikata, H. Nakano, T. Narikawa, N. Sago, H. Tagoshi, and T. Tanaka, Searching for black hole echoes from the LIGO-Virgo catalog GWTC-1, Phys. Rev. D **100**, 062006 (2019).
[71] J. Abedi, H. Dykaar, and N. Afshordi, Echoes from the abyss: Tentative evidence for planck-scale structure at black hole horizons, Phys. Rev. D **96**, 082004 (2017).
[72] G. Ashton, O. Birnholtz, M. Cabero, C. Capano, T. Dent, B. Krishnan, G. D. Meadors, A. B. Nielsen, A. Nitz, and J. Westerweck, Comments on: "echoes from the abyss: Evidence for planck-scale structure at black hole horizons", arXiv:1612.05625.
[73] M. Isi and A. J. Weinstein, Probing gravitational wave polarizations with signals from compact binary coalescences, arXiv:1710.03794.
[74] H. Takeda, S. Morisaki, and A. Nishizawa, Pure polarization test of GW170814 and GW170817 using waveforms consistent with modified theories of gravity, Phys. Rev. D **103**, 064037 (2021).
[75] H. Takeda, S. Morisaki, and A. Nishizawa, Search for scalar-tensor mixed polarization modes of gravitational waves, Phys. Rev. D **105**, 084019 (2022).
[76] K. Chatziioannou, N. Yunes, and N. Cornish, Model-independent test of general relativity: An extended post-Einsteinian framework with complete polarization content, Phys. Rev. D **86**, 022004 (2012).
[77] Y. Hagihara, N. Era, D. Iikawa, A. Nishizawa, and H. Asada, Constraining extra gravitational wave polarizations with Advanced LIGO, Advanced Virgo, and KAGRA and upper bounds from GW170817, Phys. Rev. D **100**, 064010 (2019).
[78] P. T. H. Pang, R. K. L. Lo, I. C. F. Wong, T. G. F. Li, and C. Van Den Broeck, Generic searches for alternative gravitational wave polarizations with networks of interferometric detectors, Phys. Rev. D **101**, 104055 (2020).
[79] M. Isi and L. C. Stein, Measuring stochastic gravitational-wave energy beyond general relativity, Phys. Rev. D **98**, 104025 (2018).
[80] A. Nishizawa, A. Taruya, K. Hayama, S. Kawamura, and M. Sakagami, Probing nontensorial polarizations of stochastic gravitational-wave backgrounds with ground-based laser interferometers, Phys. Rev. D **79**, 082002 (2009).
[81] T. Callister, A. S. Biscoveanu, N. Christensen, M. Isi, A. Matas, O. Minazzoli, T. Regimbau, M. Sakellariadou, J. Tasson, and E. Thrane, Polarization-based tests of gravity with the stochastic gravitational-wave background, Phys. Rev. X **7**, 041058 (2017).
[82] B. P. Abbott *et al.* (LIGO Scientific Collaboration and Virgo Collaboration), Search for tensor, vector, and scalar polarizations in the stochastic gravitational-wave background, Phys. Rev. Lett. **120**, 201102 (2018).

[83] B. Abbott, R. Abbott, T. Abbott, S. Abraham, F. Acernese, K. Ackley, C. Adams, V. Adya, C. Affeldt, M. Agathos *et al.*, Search for the isotropic stochastic background using data from Advanced LIGO's second observing run, Phys. Rev. D **100**, 061101 (2019).
[84] R. Abbott *et al.* (LIGO Scientific Collaboration, Virgo Collaboration, and KAGRA Collaboration), Upper limits on the isotropic gravitational-wave background from Advanced LIGO and Advanced Virgo's third observing run, Phys. Rev. D **104**, 022004 (2021).
[85] S. W. Ballmer, A radiometer for stochastic gravitational waves, Classical Quantum Gravity **23**, S179 (2006).
[86] S. Ballmer, LIGO interferometer operating at design sensitivity with application to gravitational radiometry, Ph.D. thesis, Massachusetts Institute of Technology, 2006.
[87] S. Mitra, S. Dhurandhar, T. Souradeep, A. Lazzarini, V. Mandic, S. Bose, and S. Ballmer, Gravitational wave radiometry: Mapping a stochastic gravitational wave background, Phys. Rev. D **77**, 042002 (2008).
[88] E. Thrane, S. Ballmer, J. D. Romano, S. Mitra, D. Talukder, S. Bose, and V. Mandic, Probing the anisotropies of a stochastic gravitational-wave background using a network of ground-based laser interferometers, Phys. Rev. D **80**, 122002 (2009).
[89] L. Tsukada, Bayesian parameter estimation for targeted anisotropic gravitational-wave background, Phys. Rev. D **107**, 023024 (2023).
[90] E. E. Flanagan, Sensitivity of the laser interferometer gravitational wave observatory to a stochastic background, and its dependence on the detector orientations, Phys. Rev. D **48**, 2389 (1993).
[91] B. Allen and A. C. Ottewill, Detection of anisotropies in the gravitational-wave stochastic background, Phys. Rev. D **56**, 545 (1997).
[92] A. K.-W. Chung and N. Yunes, Untargeted bayesian search of anisotropic gravitational-wave backgrounds through the analytical marginalization of the posterior, Phys. Rev. D **108**, 043032 (2023).
[93] J. D. Romano and N. J. Cornish, Detection methods for stochastic gravitational-wave backgrounds: A unified treatment, Living Rev. Relativity **20**, 2 (2017).
[94] B. Allen, Detecting a stochastic background of gravitational radiation: Signal processing strategies and sensitivities, Phys. Rev. D **59**, 102001 (1999).
[95] J. Suresh, A. Ain, and S. Mitra, Unified mapmaking for an anisotropic stochastic gravitational wave background, Phys. Rev. D **103**, 083024 (2021).
[96] A. Ain, J. Suresh, and S. Mitra, Very fast stochastic gravitational wave background map making using folded data, Phys. Rev. D **98**, 024001 (2018).
[97] K. M. Gorski, E. Hivon, A. J. Banday, B. D. Wandelt, F. K. Hansen, M. Reinecke, and M. Bartelman, HealPix—A Framework for high resolution discretization, and fast analysis of data distributed on the sphere, Astrophys. J. **622**, 759 (2005).
[98] A. Zonca, L. Singer, D. Lenz, M. Reinecke, C. Rosset, E. Hivon, and K. Gorski, healpy: Equal area pixelization and spherical harmonics transforms for data on the sphere in python, J. Open Source Softwaare **4**, 1298 (2019).
[99] B. P. Abbott *et al.* (LIGO Scientific Collaboration and Virgo Collaboration), Upper limits on the stochastic gravitational-wave background from advanced LIGO's first observing run, Phys. Rev. Lett. **118**, 121101 (2017).
[100] J. S. Speagle, DYNESTY: A dynamic nested sampling package for estimating Bayesian posteriors and evidences, Mon. Not. R. Astron. Soc. **493**, 3132 (2020).
[101] G. Ashton *et al.*, BILBY: A user-friendly Bayesian inference library for gravitational-wave astronomy, Astrophys. J. Suppl. Ser. **241**, 27 (2019).
[102] I. M. Romero-Shaw *et al.*, Bayesian inference for compact binary coalescences with BILBY: Validation and application to the first LIGO-Virgo gravitational-wave transient catalogue, Mon. Not. R. Astron. Soc. **499**, 3295 (2020).
[103] C. Brans and R. H. Dicke, Mach's principle and a relativistic theory of gravitation, Phys. Rev. **124**, 925 (1961).
[104] B. Abbott *et al.* (KAGRA Collabration, LIGO Scientific Collaboration, and VIRGO Collaboration), Prospects for observing and localizing gravitational-wave transients with Advanced LIGO, Advanced Virgo and KAGRA, Living Rev. Relativity **21**, 3 (2018).
[105] D. Agarwal, J. Suresh, V. Mandic, A. Matas, and T. Regimbau, Targeted search for the stochastic gravitational-wave background from the galactic millisecond pulsar population, Phys. Rev. D **106**, 043019 (2022).
[106] J. Abadie *et al.* (LIGO Scientific Collaboration and Virgo Collaboration), Directional limits on persistent gravitational waves using LIGO S5 science data, Phys. Rev. Lett. **107**, 271102 (2011).
[107] B. P. Abbott *et al.* (LIGO Scientific Collaboration and Virgo Collaboration), Directional limits on persistent gravitational waves from Advanced LIGO's first observing run, Phys. Rev. Lett. **118**, 121102 (2017).
[108] B. Abbott, R. Abbott, T. Abbott, S. Abraham, F. Acernese, K. Ackley, C. Adams, R. Adhikari, V. Adya, C. Affeldt *et al.*, Directional limits on persistent gravitational waves using data from Advanced LIGO's first two observing runs, Phys. Rev. D **100**, 062001 (2019).
[109] R. Abbott *et al.* (LIGO Scientific Collaboration, Virgo Collaboration, and KAGRA Collaboration), Search for anisotropic gravitational-wave backgrounds using data from Advanced LIGO and Advanced Virgo's first three observing runs, Phys. Rev. D **104**, 022005 (2021).